Chapter 17
Nanotribology of Ultrathin and Hard Amorphous Carbon Films

Bharat Bhushan

Abstract One of the best materials to use in applications that require very low wear and reduced friction is diamond, especially in the form of a diamond coating. Unfortunately, true diamond coatings can only be deposited at high temperatures and on selected substrates, and they require surface finishing. However, hard amorphous carbon – commonly known as diamond-like carbon or a DLC coating – has similar mechanical, thermal and optical properties to those of diamond. It can also be deposited at a wide range of thicknesses using a variety of deposition processes on various substrates at or near room temperature. The coatings reproduce the topography of the substrate, removing the need for finishing. The friction and wear properties of some DLC coatings make them very attractive for some tribological applications. The most significant current industrial application of DLC coatings is in magnetic storage devices.

In this chapter, the state-of-the-art in the chemical, mechanical and tribological characterization of ultrathin amorphous carbon coatings is presented.

EELS and Raman spectroscopies can be used to characterize amorphous carbon coatings chemically. The prevailing atomic arrangement in the DLC coatings is amorphous or quasi-amorphous, with small diamond (sp^3), graphite (sp^2) and other unidentifiable micro- or nanocrystallites. Most DLC coatings, except for those produced using a filtered cathodic arc, contain from a few to about 50 at.% hydrogen. Sometimes hydrogen is deliberately incorporated into the sputtered and ion-plated coatings in order to tailor their properties.

Amorphous carbon coatings deposited by different techniques exhibit different mechanical and tribological properties. Thin coatings deposited by filtered cathodic arc, ion beam and ECR-CVD hold much promise for tribological applications. Coatings of 5 nm or even less provide wear protection. A nanoindenter can be used to measure DLC coating hardness, elastic modulus, fracture toughness and fatigue life. Microscratch and microwear tests can be performed on the coatings using either a nanoindenter or an AFM, and along with accelerated wear testing, can be used to screen potential industrial coatings. For the examples shown in this chapter, the trends observed in such tests were similar to those found in functional tests.

B. Bhushan (ed.), *Nanotribology and Nanomechanics*,
DOI 10.1007/978-3-642-15263-4_17,

Carbon exists in both crystalline and amorphous forms and exhibits both metallic and nonmetallic characteristics [1–3]. Forms of crystalline carbon include graphite, diamond, and a family of fullerenes (Fig. 17.1). The graphite and diamond are infinite periodic network solids with a planar structure, whereas the fullerenes are a molecular form of pure carbon with a finite network and a nonplanar structure. Graphite has a hexagonal, layered structure with weak interlayer bonding forces and it exhibits excellent lubrication properties. The graphite crystal may be visualized as infinite parallel layers of hexagons stacked 0.34 nm apart with an interatomic distance of 0.1415 nm between the carbon atoms in the basal plane. Each atom lying in the basal planes is trigonally coordinated and closely packed with strong σ (covalent) bonds to its three carbon neighbors via hybrid sp^2 orbitals. The fourth electron lies in a p_z orbital lying normal to the σ bonding plane and forms a weak π bond by overlapping side-to-side with a p_z orbital of an adjacent atom to which the carbon is attached by a σ bond. The layers (basal planes) themselves are relatively far apart and the forces that bond them are weak van der Waals forces. These layers can align themselves parallel to the direction of the relative motion and slide over one another with relative ease, meaning low friction. Strong

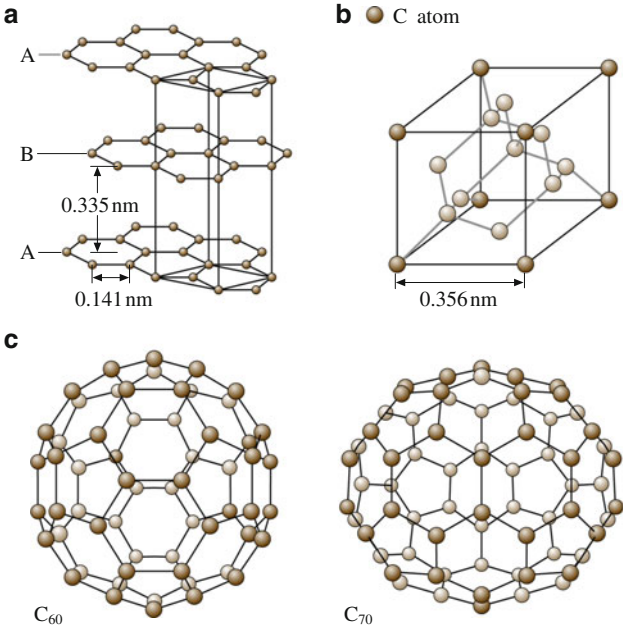

Fig. 17.1 The structures of the three known forms of crystalline carbon: **(a)** hexagonal structure of graphite, **(b)** modified face-centered cubic (fcc) structure (two interpenetrating fcc lattices displaced by a quarter of the cube diagonal) of diamond (each atom is bonded to four others that form the corners of a tetrahedron), and **(c)** the structures of the two most common fullerenes: a soccer ball C_{60} and a rugby ball C_{70} molecules

interatomic bonding and packing in each layer is thought to help reduce wear. The operating environment has a significant influence on the lubrication – low friction and low wear – properties of graphite. It lubricates better in a humid environment than a dry one, due to the adsorption of water vapor and other gases from the environment, which further weakens the interlayer bonding forces and results in easy shear and transfer of the crystallite platelets to the mating surface. Thus, transfer plays an important role in controlling friction and wear. Graphite oxidizes at high operating temperatures and can be used up to about 430°C.

One of the most well-known fullerene molecules is C_{60}, commonly known as buckyballs. Since these C_{60} molecules are very stable and do not require additional atoms to satisfy chemical bonding requirements, they are expected to have low adhesion to the mating surface and low surface energy. Since the C_{60} molecule, which has a perfect spherical symmetry, bonds only weakly to other molecules, C_{60} clusters readily become detached, similar to other layered lattice structures, and either get transferred to the mating surface by mechanical compaction or are present as loose wear particles that may roll like tiny ball bearings in a sliding contact, resulting in low friction and wear. The wear particles are expected to be harder than as-deposited C_{60} molecules, because of their phase transformation at the high-asperity contact pressures present in a sliding interface. The low surface energy, the spherical shapes of C_{60} molecules, the weak intermolecular bonding, and the high load bearing capacity offer vast potential for various mechanical and tribological applications. Sublimed C_{60} coatings and fullerene particles used as an additive to mineral oils and greases have been reported to be good solid lubricants comparable to graphite and MoS_2 [4–6].

Diamond crystallizes in a modified face-centered cubic (fcc) structure with an interatomic distance of 0.154 nm. The diamond cubic lattice consists of two interpenetrating fcc lattices displaced by a quarter of the cube diagonal. Each carbon atom is tetrahedrally coordinated, making strong σ (covalent) bonds to its four carbon neighbors using the hybrid sp^3 atomic orbitals, which accounts for it having the highest hardness (80–104 GPa) and thermal conductivity (900–2,100 W/(m K), on the order of five times that of copper) of any known solid, as well as high electrical resistivity and optical transmission and a large optical band gap. It is relatively chemically inert, and it exhibits poor adhesion with other solids, enhancing its low friction and wear properties. Its high thermal conductivity permits the dissipation of frictional heat during sliding and it protects the interface, and the dangling carbon bonds on the surface react with the environment to form hydrocarbons that act as good lubrication films. These are some of the reasons for the low friction and wear of the diamond. Diamond and its coatings find many industrial applications: tribological applications (low friction and wear), optical applications (exceptional optical transmission, high abrasion resistance), and thermal management or heat sink applications (high thermal conductivity). Diamond can be used at high temperatures; it starts to graphitize at about 1,000°C in ambient air and at about 1,400°C in vacuum. Diamond is an attractive material for cutting tools, abrasives for grinding wheels and lapping compounds, and other extreme wear applications.

Natural diamond – particularly in large quantities – is very expensive, and so diamond coatings – a low-cost alternative – are attractive. True diamond coatings are deposited by chemical vapor deposition (CVD) processes at high substrate temperatures (on the order of 800°C). They adhere best on silicon substrate and require an interlayer for other substrates. One major hindrance to the widespread use of true diamond films in tribological, optical and thermal management applications is their surface roughness. Growth of the diamond phase on a nondiamond substrate is initiated by nucleation at either randomly seeded sites or at thermally favored sites, due to statistical thermal fluctuations at the substrate surface. Depending on the growth temperature and pressure conditions, certain favored crystal orientations dominate the competitive growth process. As a result, the films grown are polycrystalline in nature with a relatively large grain size (>1μm) and they terminate in very rough surfaces, with RMS roughnesses ranging from a few tenths of a micrometer to tens of micrometers. Techniques for polishing these films have been developed. It has been reported that laser polished films exhibit friction and wear properties almost comparable to those of bulk polished diamond [7, 8].

Amorphous carbon has no long-range order, and the short-range order of the carbon atoms in it can have one or more of three bonding configurations: sp^3 (diamond), sp^2 (graphite), or sp^1 (with two electrons forming strong σ bonds, and the remaining two electrons left in orthogonal p_y and p_z orbitals, that form weak π bonds). Short-range order controls the properties of amorphous materials and coatings. Hard amorphous carbon (a-C) coatings, commonly known as diamond-like carbon or DLC (implying high hardness) coatings, are a class of coatings that are mostly metastable amorphous materials, but that include a micro- or nanocrystalline phase. The coatings are random networks of covalently bonded carbon in hybridized tetragonal (sp^3) and trigonal (sp^2) local coordination with some of the bonds terminated by hydrogen. These coatings have been successfully deposited by a variety of vacuum deposition techniques on a variety of substrates at or near room temperature. These coatings generally reproduce substrate topography and do not require any post-finishing. However, these coatings mostly adhere best on silicon substrates. The best adhesion is obtained on substrates that form carbides, such as Si, Fe and Ti. Based on depth profile analyses (using Auger and XPS) of DLC coatings deposited on silicon substrates, it has been reported that a substantial amount of silicon carbide (on the order of 5–10 nm in thickness) is present at the carbon–silicon interface, giving good adhesion and hardness [9]. For good adhesion of DLC coatings to other substrates, in most cases, an interlayer of silicon is required in most cases, except for coatings deposited by a cathodic arc.

There is significant interest in DLC coatings due to their unique combination of desirable properties. These properties include high hardness and wear resistance, chemical inertness to both acids and alkalis, lack of magnetic response, and an optical band gap ranging from zero to a few eV, depending upon the deposition conditions. These are used in a wide range of applications, including tribological, optical, electronic and biomedical applications [1, 10, 11]. The high hardness, good

friction and wear properties, versatility in deposition and substrates, and no requirement for post-deposition finishing make them very attractive for tribological applications. Two primary examples include overcoats for magnetic media (thin film disks and ME tapes) and MR-type magnetic heads for magnetic storage devices (Fig. 17.2) [12–20], and the emerging field of microelectromechanical systems (Fig. 17.3) [21–24]. The largest industrial application of the family of amorphous carbon coatings, typically deposited by DC/RF magnetron sputtering, plasma-enhanced chemical vapor deposition or ion beam deposition techniques, is in magnetic storage devices. These are employed to protect magnetic coatings on thin film rigid disks and metal evaporated tapes and the thin film head structure of a read/write disk head against wear and corrosion (Fig. 17.2). Thicknesses ranging from 3 to 10 nm are employed to maintain low physical spacing between the magnetic element of a read/write head and the magnetic layer of the storage media. Mechanical properties affect friction wear and therefore need to be optimized. In 1998, Gillette introduced Mach 3 razor blades with ultrathin DLC coatings, which could potentially become a very large industrial application. DLC coatings are also used in other commercial applications such as the glass windows of supermarket laser barcode scanners and sunglasses. These coatings are actively pursued in microelectromechanical systems (MEMS) components [23].

In this chapter, a state-of-the-art review of recent developments in the field of chemical, mechanical, and tribological characterization of ultrathin amorphous carbon coatings is presented. An overview of the most commonly used deposition techniques is provided, followed by typical chemical and mechanical characterization data and typical tribological data from both coupon-level testing and functional testing.

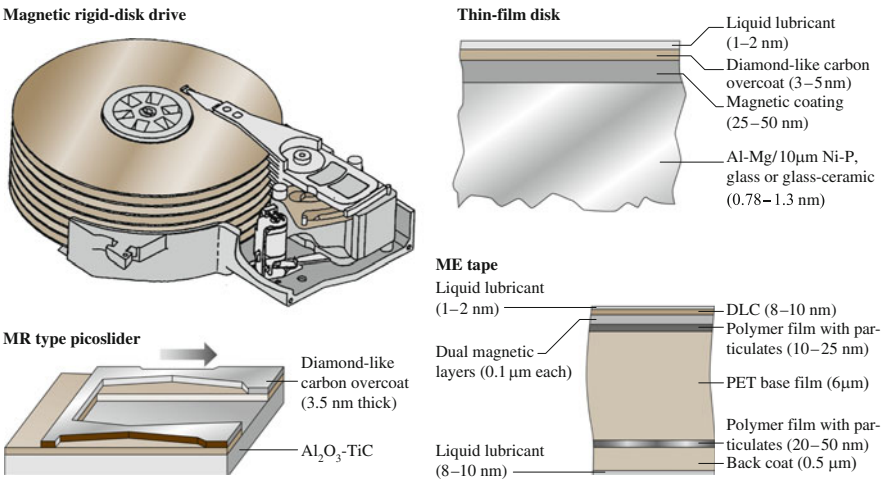

Fig. 17.2 Schematic of a magnetic rigid-disk drive and MR type picoslider, and cross-sectional schematics of a magnetic thin film rigid disk and a metal evaporated (ME) tape

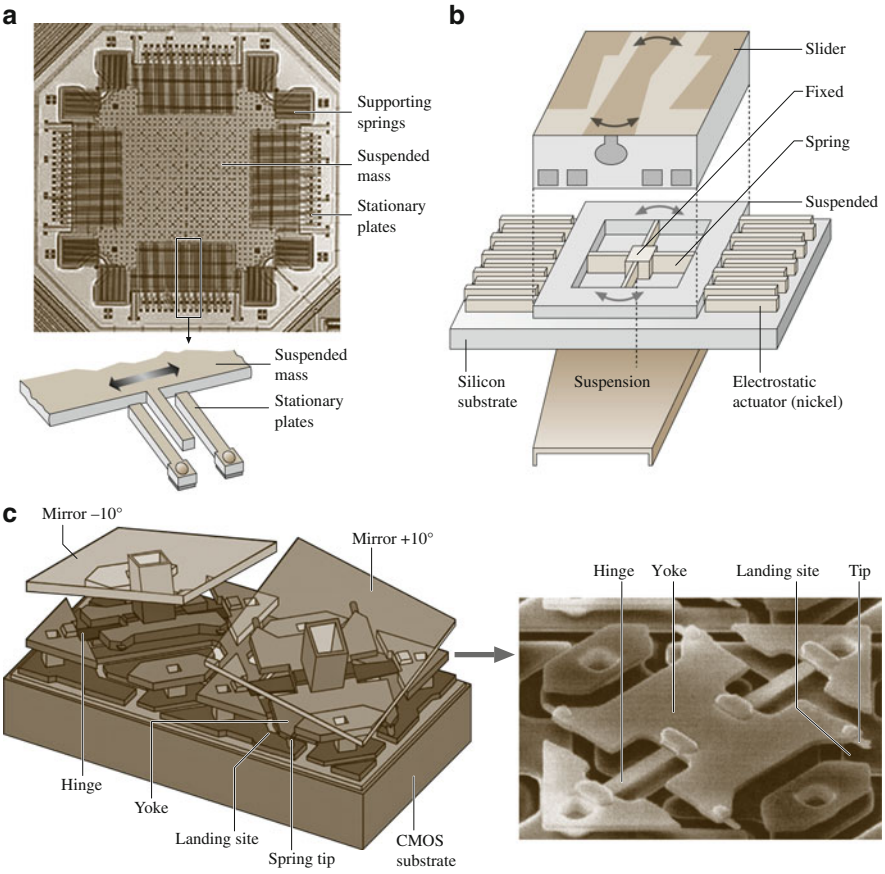

Fig. 17.3 Schematics of **(a)** a capacitive-type silicon accelerometer for automotive sensory applications, **(b)** digital micrometer devices for high-projection displays, and **(c)** a polysilicon rotary microactuator for a magnetic disk drives

17.1 Description of Common Deposition Techniques

The first hard amorphous carbon coatings were deposited by a beam of carbon ions produced in an argon plasma on room temperature substrates, as reported by Aisenberg and Chabot [25]. Subsequent confirmation by Spencer et al. [26] led to the explosive growth of this field. Following this first work, several alternative techniques were developed. Amorphous carbon coatings have been prepared by a variety of deposition techniques and precursors, including evaporation, DC, RF or ion beam sputtering, RF or DC plasma-enhanced chemical vapor deposition (PECVD), electron cyclotron resonance chemical vapor deposition (ECR-CVD), direct ion beam deposition, pulsed laser vaporization and vacuum arc, from a variety of carbon-bearing solids or gaseous source materials [1,27]. Coatings with both graphitic and

diamond-like properties have been produced. Evaporation and ion plating techniques have been used to produce coatings with graphitic properties (low hardness, high electrical conductivity, very low friction, and so on, and all of the techniques have been used to produce coatings with diamond-like properties.

The structure and properties of a coating are dependent upon the deposition technique and parameters. High-energy surface bombardment has been used to produce harder and denser coatings. It is reported that the sp^3/sp^2 fraction decreases in the order: cathodic arc deposition, pulsed laser vaporization, direct ion beam deposition, plasma-enhanced chemical vapor deposition, ion beam sputtering, DC/RF sputtering [12, 28, 29]. A common feature of these techniques is that the deposition is energetic; in other words the carbon species arrive with an energy significantly greater than that represented by the substrate temperature. The resultant coatings are amorphous in structure, with hydrogen contents of up to 50%, and display a high degree of sp^3 character. From the results of previous investigations, it has been proposed that deposition of sp^3-bonded carbon requires that the depositing species have kinetic energies on the order of 100 eV or higher, well above those obtained in thermal processes like evaporation (0–0.1 eV). The species must then be quenched into the metastable configuration via rapid energy removal. Excess energy, such as that provided by substrate heating, is detrimental to the achievement of a high sp^3 fraction. In general, the higher the fraction of sp^3-bonded carbon atoms in the amorphous network, the greater the hardness [29–36]. The mechanical and tribological properties of a carbon coating depend on the sp^3/sp^2-bonded carbon ratio, the amount of hydrogen in the coating, and the adhesion of the coating to the substrate, which are influenced by the precursor material, the kinetic energy of the carbon species prior to deposition, the deposition rate, the substrate temperature, the substrate biasing, and the substrate itself [29, 33, 35, 37–46]. The kinetic energies and deposition rates involved in selected deposition processes used in the deposition of DLC coatings are compared in Table 17.1 [1,28].

In the studies by Gupta and Bhushan [12, 47], Li and Bhushan [48, 49], and Sundararajan and Bhushan [50], DLC coatings typically ranging in thickness from 3.5 to 20 nm were deposited on single-crystal silicon, magnetic Ni-Zn ferrite, and Al_2O_3[1]-TiC substrates (surface roughness ≈1–3 nm RMS) by filtered cathodic arc (FCA) deposition, (direct) ion beam deposition (IBD), electron cyclotron resonance chemical vapor deposition (ECR-CVD), plasma-enhanced chemical vapor deposition (PECVD), and DC/RF planar magnetron sputtering (SP) deposition techniques [51]. In this chapter, we will limit the presentation of data to coatings deposited by FCA, IBD, ECR-CVD and SP deposition techniques.

17.1.1 Filtered Cathodic Arc Deposition

When the filtered cathodic arc deposition technique is used to create carbon coatings [29, 52–59], a vacuum arc plasma source is used to form the carbon film. In the FCA technique used by Gupta and Bhushan [12], energetic carbon ions are

Table 17.1 Summary of common deposition techniques, the kinetic energies of the depositing species and deposition rates

Deposition technique	Process	Kinetic energy (eV)	Deposition rate (nm/s)
Filtered cathodic arc (FCA)	Energetic carbon ions produced by a vacuum arc discharge between a graphite cathode and a grounded anode	100–2,500	0.1–1
Direct ion beam (IB)	Carbon ions produced from methane gas in an ion source and accelerated toward a substrate	50–500	0.1–1
Plasma-enhanced chemical vapor deposition (PECVD)	Hydrocarbon species produced by plasma decomposition of a hydrocarbon gas (such as acetylene) are accelerated toward a DC-biased substrate	1–30	1–10
Electron cyclotron resonance plasma chemical vapor deposition (ECR-CVD)	Hydrocarbon ions produced by the plasma decomposition of ethylene gas in the presence of a plasma at the electron cyclotron resonance condition are accelerated toward a RF-biased substrate	1–50	1–10
DC/RF sputtering	Sputtering of graphite target by argon ion plasma	1–10	1–10

produced by a vacuum arc discharge between a planar graphite cathode and a grounded anode (Fig. 17.4a). The cathode is a 6 mm diameter high-density graphite disk mounted on a water-cooled copper block. The arc is driven at an arc current of 200 A, with an arc duration of 5 ms and an arc repetition rate of 1 Hz. The plasma beam is guided by a magnetic field that transports current between the electrodes to form tiny, rapidly moving spots on the cathode surface. The source is coupled to a 90° bent magnetic filter to remove the macroparticles produced concurrently with the plasma in the cathode spots. The ion current density at the substrate is in the range of 10–50 mA/cm^2. The base pressure is less than 10^{-4} Pa. A much higher plasma density is achieved using a powerful arc discharge than using electron beam evaporation with auxiliary discharge. In the discharge process, the cathodic material suffers a complicated transition from the solid phase to an expanding, nonequilibrium plasma via liquid and dense equilibrium nonideal plasma phases [58]. The carbon ions in the vacuum arc plasma have a direct kinetic energy of 20–30 eV. The high voltage pulses are applied to the substrate which is mounted on a water-cooled sample holder, and ions are accelerated through the sheath and arrive at the substrate with an additional energy given by the potential difference between the plasma and the substrate. The substrate holder is pulsed-biased to a voltage of up to -2 kV with a pulse duration of 1 μs. The negative biasing of -2 kV corresponds to a kinetic energy of 2 keV for the carbon ions. The use of a pulsed bias instead of a DC bias enables much higher voltages to be applied and it permits a surface potential to be created on nonconducting films. The ion energy is varied during

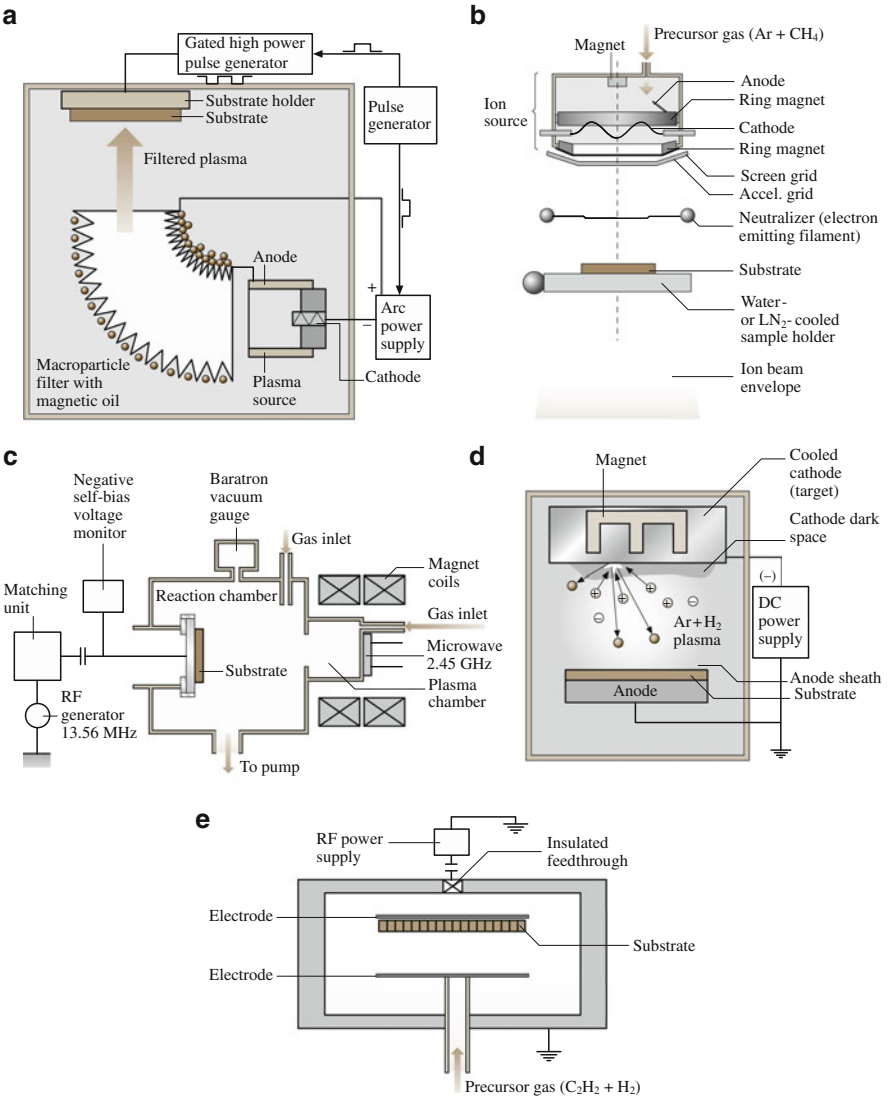

Fig. 17.4 Schematic diagrams of deposition by **(a)** filtered cathodic arc deposition, **(b)** ion beam deposition, **(c)** electron cyclotron resonance chemical vapor deposition (ECR-CVD), **(d)** DC planar magnetron sputtering, and **(e)** plasma-enhanced chemical vapor deposition (PECVD)

the deposition. For the first 10% of the deposition, the substrates are pulsed-biased to −2 keV with a pulse duty cycle of 25%, so for 25% of the time the energy is 2 keV and for the remaining 75% it is 20 eV, which is the *natural* energy of carbon ions in a vacuum discharge. For the last 90% of the deposition, the pulsed-biased voltage is reduced to −200 eV with a pulsed bias duty cycle of 25%, so the energy is 200 eV for 25% and 20 eV for 75% of the deposition. The high energy at the

beginning leads to good intermixing and adhesion of the films, whereas the lower energy at the later stage leads to hard films. Under the conditions described, the deposition rate at the substrate is about 0.1 nm/s, which is slow. Compared with most gaseous plasma, the cathodic arc plasma is almost fully ionized, and the ionized carbon atoms have high kinetic energies which promotes the formation of a high fraction of sp^3-bonded carbon ions, which in turn results in high hardness and higher interfacial adhesion. Cuomo et al. [42] have reported, based on electron energy loss spectroscopy (EELS) analysis, that the sp^3-bonded carbon fraction of a cathodic arc coating is 83% compared to 38% for ion beam sputtered carbon. These coatings are reported to be *nonhydrogenated*.

This technique does not require an adhesion underlayer for nonsilicon substrates. However, adhesion of the DLC coatings on the electrically insulating substrate is poor, as negative pulsed biasing forms an electrical sheath that accelerates depositing ions to the substrate and enhances the adhesion of the coating to the substrate with associated ion implantation. It is difficult to build potential on an insulating substrate, and lack of biasing results in poor adhesion.

17.1.2 Ion Beam Deposition

In the direct ion beam deposition of a carbon coating [60–64], as used by Gupta and Bhushan [12], the carbon coating is deposited from an accelerated carbon ion beam. The sample is precleaned by ion etching. In the case of nonsilicon substrates, a 2–3 nm thick amorphous silicon adhesion layer is deposited by ion beam sputtering using an ion beam containing a mixture of methane and argon at 200 V. For the carbon deposition, the chamber is pumped to about 10^{-4} Pa, and methane gas is fed through the cylindrical ion source and ionized by energetic electrons produced by a hot-wire filament (Fig. 17.4b). Ionized species then pass through a grid with a bias voltage of about 50 eV, where they gain a high acceleration energy and reach a hot-wire filament, emitting thermionic electrons that neutralize the incoming ions. The discharging of ions is important when insulating ceramics are used as substrates. The species are then deposited on a water-cooled substrate. Operating conditions are adjusted to give an ion beam with an acceleration energy of about 200 eV and a current density of about 1 mA/cm^2. At these operating conditions, the deposition rate is about 0.1 nm/s, which is slow. Incidentally, tough and soft coatings are deposited at a high acceleration energy of about 400 eV and at a deposition rate of about 1 nm/s. The ion beam-deposited carbon coatings are reported to be hydrogenated (30–40at.% hydrogen).

17.1.3 Electron Cyclotron Resonance Chemical Vapor Deposition

The lack of electrodes in the ECR-CVD technique and its ability to create high densities of charged and excited species at low pressures ($\leq 10^{-4}$ Torr) make it

attractive for coating deposition [65]. In the ECR-CVD carbon deposition process described by Suzuki and Okada [66] and used by Li and Bhushan [48, 49] and Sundararajan and Bhushan [50], microwave power is generated by a magnetron operating in continuous mode at a frequency of 2.45 GHz (Fig. 17.4c). The plasma chamber functions as a microwave cavity resonator. The magnetic coils arranged around the plasma chamber generate a magnetic field of 875 G, necessary for electron cyclotron resonance. The substrate is placed on a stage that is connected capacitively to a 13.56 MHz RF generator. The process gas is introduced into the plasma chamber and the hydrocarbon ions generated are accelerated by a negative self-bias voltage, which is generated by applying RF power to the substrate. Both the substrate stage and the plasma chamber are water-cooled. The process gas used is 100% ethylene and its flow rate is held constant at 100 sccm. The microwave power is 100–900 W. The RF power is 30–120 W. The pressure during deposition is kept close to the optimum value of 5.5×10^{-3} Torr. Before the deposition, the substrates are cleaned using Ar ions generated in the ECR plasma chamber.

17.1.4 Sputtering Deposition

In DC planar magnetron carbon sputtering [13, 33, 37, 40, 67–71], the carbon coating is deposited by the sputtering of a graphite target with Ar ion plasma. In the glow discharge, positive ions from the plasma strike the target with sufficient energy to dislodge the atoms by momentum transfer, which are intercepted by the substrate. An ≈5 nm thick amorphous silicon adhesion layer is initially deposited by sputtering if the deposition is to be carried out on a nonsilicon surface. In the process used by Gupta and Bhushan [12], the coating is deposited by the sputtering of a 200 mm diameter graphite target with Ar ion plasma at 300 W power and a pressure of about 0.5 Pa (6 mTorr) (Fig. 17.4d). Plasma is generated by applying a DC potential between the substrate and a target. Bhushan et al. [35] reported that the sputtered carbon coating contains about 35 at.% hydrogen. The hydrogen comes from the hydrocarbon contaminants present in the deposition chamber. In order to produce a hydrogenated carbon coating with a larger concentration of hydrogen, the deposition is carried out in Ar and hydrogen plasma.

17.1.5 Plasma-Enhanced Chemical Vapor Deposition

In the RF-PECVD deposition of carbon, as used by Gupta and Bhushan [12], the carbon coating is deposited by adsorbing hydrocarbon free radicals onto the substrate and then via chemical bonding to other atoms on the surface. The hydrocarbon species are produced by the RF plasma decomposition of hydrocarbon precursors such as acetylene (C_2H_2), Fig. 17.4e [27, 69, 72–75]. Instead of requiring thermal energy, as in thermal CVD, the energetic electrons in the plasma (at

a pressure of 1–5×10^2 Pa, and typically less than 10 Pa) can activate almost any reaction among the gases in the glow discharge at relatively a low substrate temperature of 100–600°C (typically less than 300°C). To deposit the coating on nonsilicon substrates, an amorphous silicon adhesion layer about 4 nm thick is first deposited under similar conditions from a gas mixture of 1% silane in argon in order to improve adhesion [76]. In the process used by Gupta and Bhushan [12], the plasma is sustained in a parallel-plate geometry by a capacitive discharge at 13.56 MHz, at a surface power density of around 100 mW/cm^2. The deposition is performed at a flow rate on the order of 6 sccm and a pressure on the order of 4 Pa (30 mTorr) on a cathode-mounted substrate maintained at a substrate temperature of 180°C. The cathode bias is held fixed at about −120 V with an external DC power supply attached to the substrate (powered electrode). The carbon coatings deposited by PECVD usually contain hydrogen at levels of up to 50% [35, 77].

17.2 Chemical and Physical Coating Characterization

The chemical structures and properties of amorphous carbon coatings depend on the deposition conditions employed when they are formed. It is important to understand the relationship between the chemical structure of a coating and its properties since it allows useful deposition parameters to be defined. Amorphous carbon films are metastable phases formed when carbon particles are condensed on a substrate. The prevailing atomic arrangement in the DLC coatings is amorphous or quasi-amorphous, with small diamond (sp^3), graphite (sp^2) and other unidentifiable micro- or nanocrystallites. The coating is dependent upon the deposition process and the deposition conditions used because these influence the sp^3/sp^2 ratio and the proportion of hydrogen in the coating. The sp^3/sp^2 ratios of DLC coatings typically range from 50% to close to 100%, and hardness increases with the sp^3/sp^2 ratio. Most DLC coatings, except those produced by a filtered cathodic arc, contain from a few to about 50% a*t*. hydrogen. Sometimes hydrogen and nitrogen are deliberately added to produce hydrogenated (a-C:H) and nitrogenated amorphous carbon (a-C:N) coatings, respectively. Hydrogen helps to stabilize sp^3 sites (most of the carbon atoms attached to hydrogen have a tetrahedral structure), so the sp^3/sp^2 ratio for hydrogenated carbon is higher [30]. The optimum sp^3/sp^2 ratio for a random covalent network composed of sp^3 and sp^2 carbon sites (N_{sp^2} and N_{sp^3}) and hydrogen is [30]

$$\frac{N_{sp^3}}{N_{sp^2}} = \frac{6X_H - 1}{8 - 13X_H}, \tag{17.1}$$

where X_H is the atomic fraction of hydrogen. The hydrogenated carbon has a larger optical band gap, higher electrical resistivity (semiconductor), and a lower optical absorption or high optical transmission. Hydrogenated coatings have lower

densities, probably because of the reduced cross-linking due to hydrogen incorporation. However, the hardness decreases with increasing hydrogen, even though the proportion of sp^3 sites increases (that is, as the local bonding environment becomes more diamondlike) [78, 79]. It is speculated that the high hydrogen content introduces frequent terminations in the otherwise strong 3-D network, and hydrogen increases the soft polymeric component of the structure more than it enhances the cross-linking sp^3 fraction.

A number of investigations have been performed to identify the microstructure of amorphous carbon films using a variety of techniques, such as Raman spectroscopy, EELS, nuclear magnetic resonance, optical measurements, transmission electron microscopy, and x-ray photoelectron spectroscopy [33]. The structure of diamondlike amorphous carbon is amorphous or quasi-amorphous, with small graphitic (sp^2), tetrahedrally coordinated (sp^3) and other types of nanocrystallites (typically on the order of a couple of nm in size, randomly oriented) [33, 80, 81]. These studies indicate that the chemical structure and physical properties of the coatings are quite variable, depending on the deposition techniques and film growth conditions. It is clear that both sp^2- and sp^3-bonded atomic sites are incorporated in diamondlike amorphous carbon coatings and that the physical and chemical properties of the coatings depend strongly on their chemical bonding and microstructures. Systematic studies have been conducted to carry out chemical characterization and to investigate how the physical and chemical properties of amorphous carbon coatings vary as a function of deposition conditions [33, 35, 40]. EELS and Raman spectroscopy are commonly used to characterize the chemical bonding and microstructure. The hydrogen concentration in the coating is obtained via forward recoil spectrometry (FRS). A variety of physical properties relevant to tribological performance are measured.

In order to give the reader a feel for typical data obtained when characterizing amorphous carbon coatings and their relationships to physical properties, we present data on several sputtered coatings, RF-PECVD amorphous carbon and microwave-PECVD (MPECVD) diamond coatings [33, 35, 40]. The sputtered coatings were DC magnetron sputtered at a chamber pressure of 10 mTorr under sputtering power densities of 0.1 and 2.1 W/cm^2 (labeled as coatings W1 and W2, respectively) in a pure Ar plasma. These coatings were prepared at a power density of 2.1 W/cm^2 with various hydrogen fractions (0.5, 1, 3, 5, 7 and 10%) of Ar/H; the gas mixtures were labeled as H1, H2, H3, H4, H5, and H6, respectively.

17.2.1 EELS and Raman Spectroscopy

EELS and Raman spectra of four sputtered (W1, W2, H1, and H3) carbon samples and one PECVD carbon sample were obtained. Figure 17.5 shows the EELS spectra of these carbon coatings. EELS spectra (up to 50 eV) for bulk diamond and polycrystalline graphite are also shown in Fig. 17.5. One prominent peak is seen

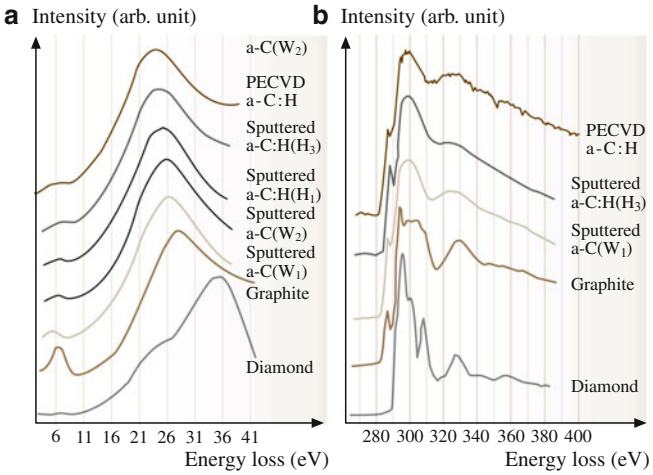

Fig. 17.5 **(a)** Low-energy and **(b)** high-energy EELS of DLC coatings produced by the DC magnetron sputtering and RF-PECVD techniques. Data for bulk diamond and polycrystalline graphite are included for comparison [35]

at 35 eV in diamond, while two peaks are seen at 27 eV and 6.5 eV in graphite, which are called the ($\pi + \sigma$) and (π) peaks, respectively. These peaks are produced by the loss of transmitted electron energy to plasmon oscillations of the valence electrons. The $\pi + \sigma$ peak in each coating is positioned at a lower energy region than that of graphite. The π peaks in the W series and PECVD samples also occur at a lower energy region than that of the graphite. However, the π peaks in the H-series are comparable to or higher than those of graphite (Table 17.2). The plasmon oscillation frequency is proportional to the square root of the corresponding electron density to a first approximation. Therefore, the samples in the H-series most likely have a higher density of π electrons than the other samples.

Amorphous carbon coatings contain (mainly) a mixture of sp^2- and sp^3-bonds, even though there is some evidence for the presence of *sp*-bonds as well [82]. The PECVD coatings and the H-series coatings in this study have almost the same mass density (as seen in Table 17.4, discussed in more detail later), but the former have a lower concentration of hydrogen (18.1%) than the H-series (35–39%) (as seen in Table 17.3, also discussed in more detail later). The relatively low-energy positions of the π peaks of the PECVD coatings compared to those of the H-series indicates that the PECVD coatings contain a higher fraction of sp^3-bonds than the sputtered hydrogenated carbon coatings (H-series).

Figure 17.5b shows EELS spectra associated with the inner-shell (K-shell) ionization. Again, the spectra for diamond and polycrystalline graphite are included for comparison. Sharp peaks are observed at 285.5 eV and 292.5 eV in graphite, while no peak is seen at 285.5 eV in diamond. The general features of the K-shell EELS spectra for the sputtered and PECVD carbon samples resemble those of graphite, but with the higher energy features smeared. The peak at 285.5 eV in the

Table 17.2 Experimental results from EELS and Raman spectroscopy [35]

Sample	EELS peak position		Raman peak position		Raman FWHM[a]		I_D/I_G[d]
	π (eV)	$\pi + \sigma$ (eV)	G-band[b] (cm^{-1})	D-band[c] (cm^{-1})	G-band (cm^{-1})	D-band (cm^{-1})	
Sputtered a-C coating (W1)	5.0	24.6	1,541	1,368	105	254	2.0
Sputtered a-C coating (W2)	6.1	24.7	1,560	1,379	147	394	5.3
Sputtered a-C:H coating (H1)	6.3	23.3	1,542	1,334	95	187	1.6
Sputtered a-C:H coating (H3)	6.7	22.4	e	e	e	e	e
PECVD a-C:H coating	5.8	24.0	1,533	1,341	157	427	1.5
Diamond coating	–	–	1,525[f]	1,333[g]	–	8[g]	–
Graphite (for reference)	6.4	27.0	1,580	1,358	37	47	0.7
Diamond (for reference)	–	37.0	–	1,332[g]	–	2[g]	–

[a]Full width at half maximum
[b]Peak associated with sp^2 *graphite* carbon
[c]Peak associated with sp^2 *disordered* carbon (not sp^3-bonded carbon)
[d]Intensity ratio of the D-band to the G-band
[e]Fluorescence
[f]Includes D- and G-band, signal too weak to analyze
[g]Peak position and width for diamond phonon

Table 17.3 Experimental results of FRS analysis [35]

Sample	Ar/H ratio	C (at.% ± 0.5)	H (at.% ± 0.5)	Ar (at.% ± 0.5)	O (at.% ± 0.5)
Sputtered a-C coating (W2)	100/0	90.5	9.3	0.2	–
Sputtered a-C:H coating (H2)	99/1	63.9	35.5	0.6	–
Sputtered a-C:H coating (H3)	97/3	56.1	36.5	–	7.4
Sputtered a-C:H coating (H4)	95/5	53.4	39.4	–	7.2
Sputtered a-C:H coating (H5)	93/7	58.2	35.4	0.2	6.2
Sputtered a-C:H coating (H6)	90/10	57.3	35.5	–	7.2
PECVD a-C:H coating	99.5% CH_4	81.9	18.1	–	–
Diamond coating	H_2-1 mol % CH_4	94.0	6.0	–	–

sputtered and PECVD coatings also indicates the presence of sp^2-bonded atomic sites in the coatings. All of these spectra peak at 292.5 eV, similar to the spectra of graphite, but the peak in graphite is sharper.

Raman spectra from samples W1, W2, H1 and PECVD are shown in Fig. 17.6. Raman spectra could not be observed in specimens H2 and H3 due to high fluorescence signals. The Raman spectra of single-crystal diamond and polycrystalline graphite are also shown for comparison in Fig. 17.6. The results from the spectral fits are summarized in Table 17.2. We will focus on the position of the

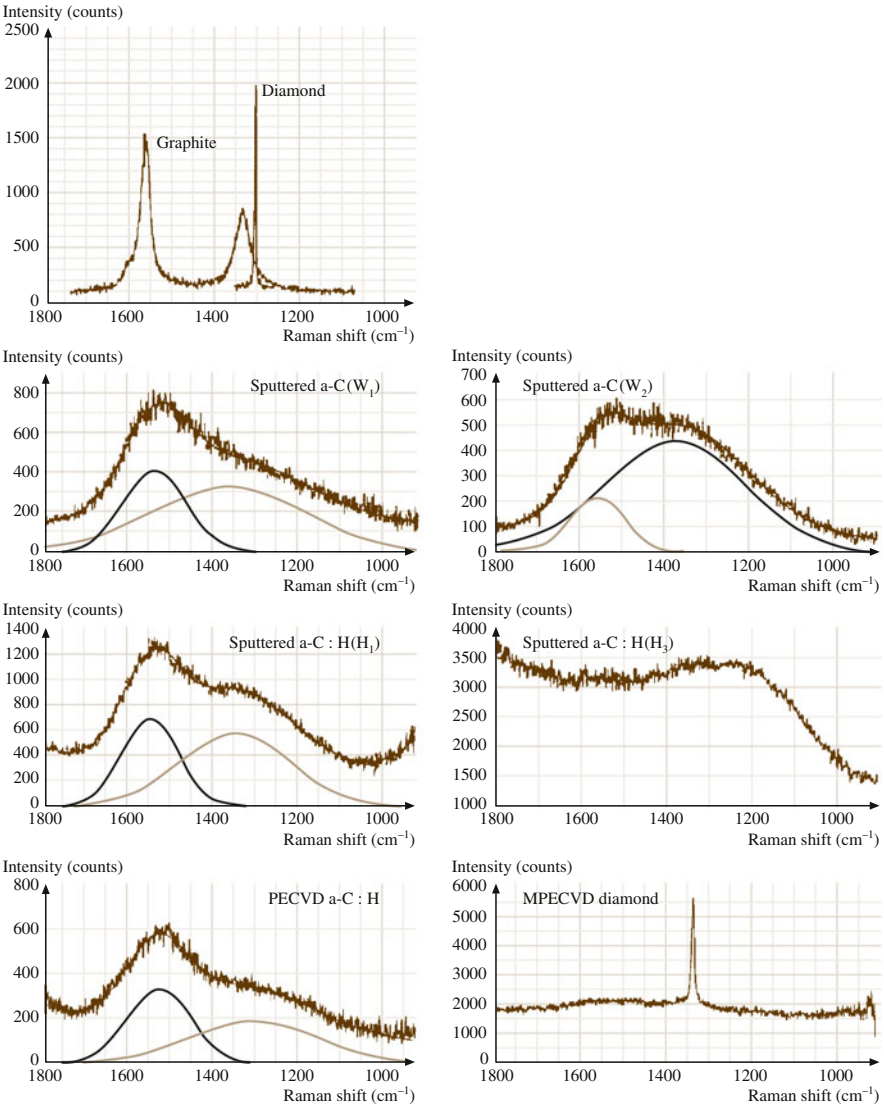

Fig. 17.6 Raman spectra of the DLC coatings produced by DC magnetron sputtering and RF-PECVD techniques and a diamond film produced by the MPE-CVD technique. Data for bulk diamond and microcrystalline graphite are included for comparison [35]

G-band, which has been shown to be related to the fraction of sp^3-bonded sites. Increasing the power density in the amorphous carbon coatings (W1 and W2) results in a higher G-band frequency, implying a smaller fraction of sp^3-bonding in W2 than in W1. This is consistent with the higher density of W1. H1 and PEVCD have even lower G-band positions than W1, implying an even higher fraction of sp^3-bonding, which is presumably caused by the incorporation of H atoms into the lattice. The high hardness of H3 might be attributed to efficient sp^3 cross-linking of small sp^2-ordered domains.

The Raman spectrum of a MPECVD diamond coating is shown in Fig. 17.6. The Raman peak of diamond is at 1,333 cm^{-1}, with a line width of 7.9 cm^{-1}. There is a small broad peak at around 1,525 cm^{-1}, which is attributed to a small amount of a-C:H. This impurity peak is not intense enough to be able to separate the G- and D-bands. The diamond peak frequency is very close to that of natural diamond (1,332.5 cm^{-1}, see Fig. 17.6), indicating that the coating is not under stress [83]. The large line width compared to that of natural diamond (2 cm^{-1}) indicates that the microcrystallites probably have a high concentration of defects [84].

17.2.2 Hydrogen Concentrations

A FRS analysis of six sputtered (W2, H2, H3, H4, H5, and H6) coatings, one PECVD coating, and one diamond coating was performed. Figure 17.7 shows an overlay of the spectra from the six sputtered samples. Similar spectra were obtained from the PECVD and the diamond films. Table 17.3 shows the H and C fractions as well as the amount of impurities (Ar and O) in the films in atomic %. Most apparent is the large fraction of H in the sputtered films. Regardless of how much H_2 is in the Ar sputtering gas, the H content of the coatings is about the same, $\approx$ 35 at.%.

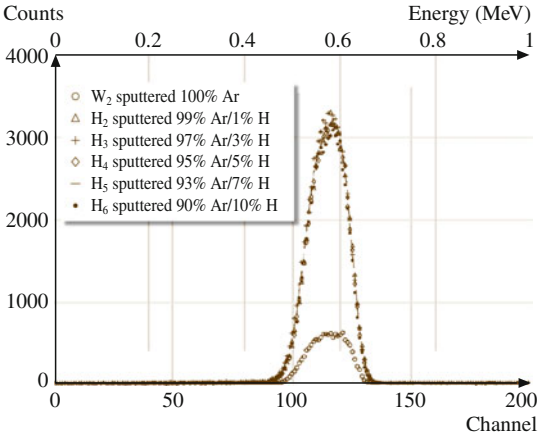

Fig. 17.7 FRS spectra for six DLC coatings produced by DC magnetron sputtering [35]

Interestingly, there is still ≈ 10% H present in the coating sputtered in pure Ar (W2). It is interesting to note that Ar is present only in coatings grown using Ar carrier gas with a low (<1%) H content. The presence of O in the coatings combined with the fact that the coatings were prepared approximately nine months before the FRS analysis caused suspicion that they had absorbed water vapor, and that this may be the cause of the H peak in specimen W2.

All samples were annealed for 24 h at 250°C in a flowing He furnace and then reanalyzed. Surprisingly, the H contents of all coatings measured increased slightly, even though the O content decreased, and W2 still had a substantial amount of H_2. This slight increase in H concentration is not understood. However, the fact that the H concentration did not decrease with the oxygen as a result of annealing suggests that high H concentration is not due to adsorbed water vapor. The PECVD film has more H (≈ 18%) than the sputtered films initially, but after annealing it has the same fraction as specimen W2, the film sputtered in pure Ar. The diamond film has the smallest amount of hydrogen, as seen in Table 17.3.

17.2.3 Physical Properties

The physical properties of the four sputtered (W1, W2, H1, and H3) coatings, one PECVD coating, one diamond coating, and bulk diamond and graphite are presented in Table 17.4. The hydrogenated carbon and the diamond coatings have very high resistivity compared to unhydrogenated carbon coatings. It appears that

Table 17.4 Experimental results of physical properties [35]

Sample	Mass density (g/cm^3)	Nano-hardness (GPa)	Elastic modulus (GPa)	Electrical resistivity (Ω cm)	Compressive residual stress (GPa)
Sputtered a-C coating (W1)	2.1	15	141	1,300	0.55
Sputtered a-C:H coating (W2)	1.8	14	136	0.61	0.57
Sputtered a-C:H coating (H1)	–	14	96	–	> 2
Sputtered a-C:H coating (H3)	1.7	7	35	$> 10^6$	0.3
PECVD a-C:H coating	1.6–1.8	33–35	≈ 200	$> 10^6$	1.5–3.0
Diamond coating	–	40–75	370–430	–	–
Graphite (for reference)	2.267	Soft	9–15	5×10^{-5a}, 4×10^{-3b}	0
Diamond (for reference)	3.515	70–102	900–1,050	10^7–10^{20}	0

[a]Parallel to layer planes
[b]Perpendicular to layer planes

unhydrogenated carbon coatings have higher densities than hydrogenated carbon coatings, although both groups are less dense than graphite. The density depends upon the deposition technique and the deposition parameters. It appears that unhydrogenated sputtered coatings deposited at low power exhibit the highest density. The nanohardness of hydrogenated carbon is somewhat lower than that of unhydrogenated carbon. PECVD coatings are significantly harder than sputtered coatings. The nanohardness and modulus of elasticity of a diamond coating is very high compared to that of a DLC coating, even though the hydrogen contents are similar. The compressive residual stresses of the PECVD coatings are substantially higher than those of sputtered coatings, which is consistent with the results for the hardness.

Figure 17.8a shows the effect of hydrogen in the plasma on the residual stresses and the nanohardness for the sputtered coatings W2 and H1 to H6. The coatings made with a hydrogen flow of between 0.5 and 1.0% delaminate very quickly, even when they are only a few tens of nm thick. In pure Ar and at H_2 flows that are greater than 1%, the coatings appear to be more adhesive. The tendency of some coatings to delaminate can be caused by intrinsic stress in the coating, which is measured by substrate bending. All of the coatings in the figure are in compressive stress. The maximum stress occurs between 0 and 1% H_2 flow, but the stress cannot be quantified in this range because the coatings instantly delaminate upon exposure to air. At higher hydrogen concentrations the stress gradually

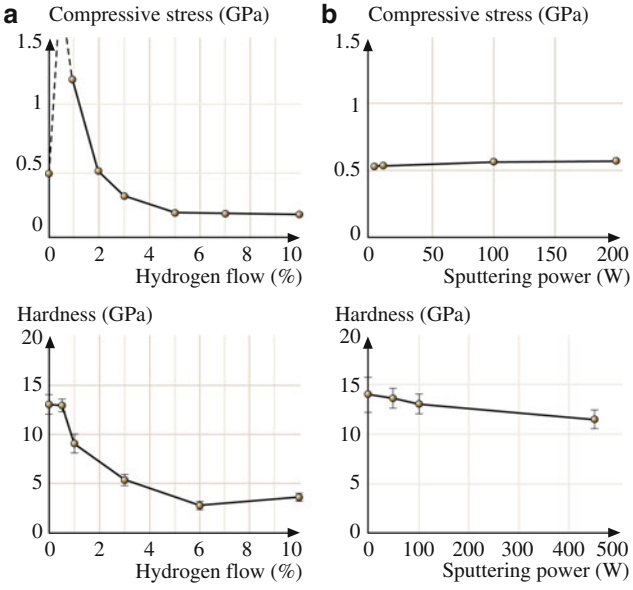

Fig. 17.8 Residual compressive stresses and nanohardness **(a)** as a function of hydrogen flow rate, where the sputtering power is 100 W and the target diameter is 75 mm (power density = 2.1 W/cm^2), and **(b)** as a function of sputtering power over a 75 mm diameter target with no hydrogen added to the plasma [40]

diminishes. A generally decreasing trend is observed for the hardness of the coatings as the hydrogen content is increased. The hardness decreases slightly, going from 0% H_2 to 0.5% H_2, and then decreases sharply. These results are probably lower than the true values because of local delamination around the indentation point. This is especially likely for the 0.5% and 1.0% coatings, where delamination is visually apparent, but may also be true to a lesser extent for the other coatings. Such an adjustment would bring the hardness profile into closer correlation with the stress profile. Weissmantel et al. [68] and Scharff et al. [85] observed a downturn in hardness for high bias and a low hydrocarbon gas pressure for ion-plated carbon coating, and, therefore, presumably low hydrogen content in support of the above contention.

Figure 17.8b shows the effect of sputtering power (with no hydrogen added to the plasma) on the residual stresses and nanohardness for various sputtered coatings. As the power decreases, the compressive stress does not seem to change while the nanohardness slowly increases. The rate of change becomes more rapid at very low power levels.

The addition of H_2 during sputtering of the carbon coatings increases the H concentration in the coating. Hydrogen causes the character of the C–C bonds to shift from sp^2 to sp^3, and a rise in the number of C–H bonds, which ultimately relieves stress and produces a softer *polymerlike* material. Low power deposition, like the presence of hydrogen, appears to stabilize the formation of sp^3 C–C bonds, increasing hardness. These coatings relieve stress and lead to better adhesion. Increasing the temperature during deposition at high power density results in graphitization of the coating material, producing a decrease in hardness with an increase in power density. Unfortunately, low power also means impractically low deposition rates.

17.2.4 Summary

Based on analyses of EELS and Raman data, it is clear that all DLC coatings have both sp^2 and sp^3 bonding characteristics. The sp^2/sp^3 bonding ratio depends upon the deposition technique and parameters used. DLC coatings deposited by sputtering and PECVD contain significant concentrations of hydrogen, while diamond coatings contain only small amounts of hydrogen impurities. Sputtered coatings with no deliberate addition of hydrogen in the plasma contain a significant amount of hydrogen. Regardless of how much hydrogen is in the Ar sputtering gas, the hydrogen content of the coatings increases initially but then does not increase further.

Hydrogen flow and sputtering power density affect the mechanical properties of these coatings. Maximum compressive residual stress and hardness occur between 0 and 1% hydrogen flow, resulting in rapid delamination. Low sputtering power moderately increases hardness and also relieves residual stress.

17.3 Micromechanical and Tribological Coating Characterization

17.3.1 Micromechanical Characterization

Common mechanical characterizations include measurements of hardness and elastic modulus, fracture toughness, fatigue life, and scratch and wear testing. Nanoindentation and atomic force microscopy (AFM) are used for the mechanical characterization of ultrathin films.

Hardness and elastic modulus are calculated from the load displacement data obtained by nanoindentation at loads of typically 0.2–10 mN using a commercially available nanoindenter [23, 86]. This instrument monitors and records the dynamic load and displacement of the three-sided pyramidal diamond (Berkovich) indenter during indentation. For fracture toughness measurements of ultrathin films 100 nm to a few μm thick, a nanoindentation-based technique is used in which through-thickness cracking in the coating is detected from a discontinuity observed in the load–displacement curve, and the energy released during the cracking is obtained from the curve [87–89]. Based on the energy released, fracture mechanics analysis is then used to calculate the fracture toughness. An indenter with a cube-corner tip geometry is preferred because the through-thickness cracking of hard films can be accomplished at lower loads. In fatigue measurement, a conical diamond indenter with a tip radius of about 1 μm is used and load cycles with sinusoidal shapes are applied [90, 91]. The fatigue behavior of a coating is studied by monitoring the change in contact stiffness, which is sensitive to damage formation.

Hardness and Elastic Modulus

For materials that undergo plastic deformation, high hardness and elastic modulus are generally needed for low friction and wear, whereas for brittle materials, high fracture toughness is needed [2, 3, 21]. The DLC coatings used for many applications are hard and brittle, and values of hardness and fracture toughness need to be optimized.

Representative load–displacement plots of indentations made at 0.2 mN peak indentation load on 100 nm thick DLC coatings deposited by the four deposition techniques on a single-crystal silicon substrate are compared in Fig. 17.9. The indentation depths at the peak load range from about 18 to 26 nm, smaller than that of the coating thickness. Many of the coatings exhibit a discontinuity or pop-in marks in the loading curve, which indicate a sudden penetration of the tip into the sample. A nonuniform penetration of the tip into a thin coating possibly results from formation of cracks in the coating, formation of cracks at the coating–substrate interface, or debonding or delamination of the coating from the substrate.

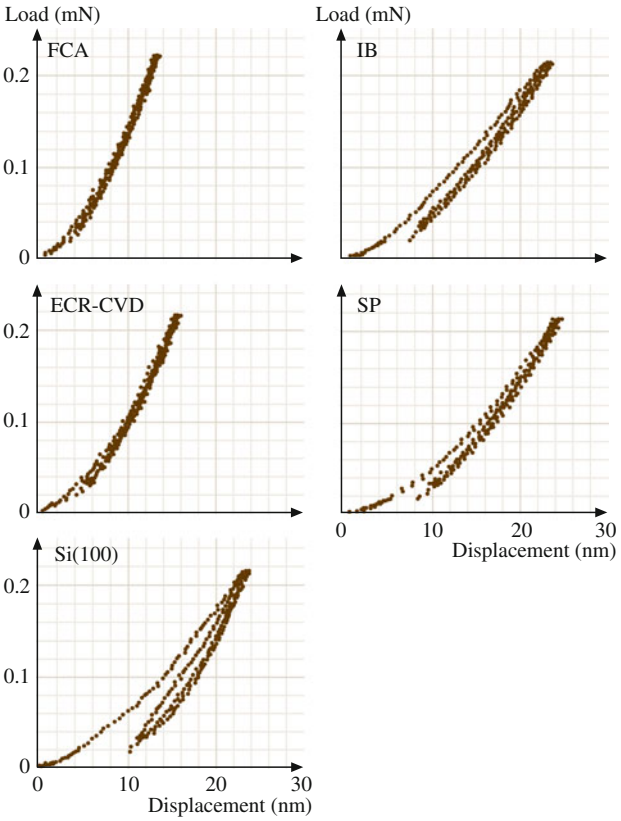

Fig. 17.9 Load versus displacement plots for various 100 nm thick amorphous carbon coatings on single-crystal silicon substrate and bare substrate

The hardness and elastic modulus values for a peak load of 0.2 mN on the various coatings and single-crystal silicon substrate are summarized in Table 17.5 and Fig. 17.10 [47, 49, 89, 90]. Typical values for the peak and residual indentation depths range from 18 to 26 nm and 6 to 12 nm, respectively. The FCA coating exhibits the greatest hardness of 24 GPa and the highest elastic modulus of 280 GPa of the various coatings, followed by the ECR-CVD, IB and SP coatings. Hardness and elastic modulus have been known to vary over a wide range with the sp^3-to-sp^2 bonding ratio, which depends on the kinetic energy of the carbon species and the amount of hydrogen [6, 30, 47, 92, 93]. The high hardness and elastic modulus of the FCA coatings are attributed to the high kinetic energy of the carbon species involved in the FCA deposition [12, 47]. Anders et al. [57] also reported a high hardness, measured by nanoindentation, of about 45 GPa for cathodic arc carbon coatings. They observed a change in hardness from 25 to 45 GPa with a pulsed bias voltage and bias duty cycle. The high hardness of cathodic arc carbon was attributed to the high percentage (more than 50%) of sp^3 bonding. Savvides and

Table 17.5 Hardness, elastic modulus, fracture toughness, fatigue life, critical load during scratch, coefficient of friction during accelerated wear testing and residual stress for various DLC coatings on single-crystal silicon substrate

Coating	Hardness[a] [48] (GPa)	Elastic modulus[a] [48] (GPa)	Fracture toughness[a] [89] (MPa $m^{1/2}$)	Fatigue life[b] N_f[d] [90] $\times 10^4$	Critical load during scratch[b] [48] (mN)	Coefficient of friction during accelerated wear testing[b] [48]	Compressive residual stress[c] [47] (GPa)
Cathodic arc carbon coating (a-C)	24	280	11.8	2.0	3.8	0.18	12.5
Ion beam carbon coating (a-C:H)	19	140	4.3	0.8	2.3	0.18	1.5
ECR-CVD carbon coating (a-C:H)	22	180	6.4	1.2	5.3	0.22	0.6
DC sputtered carbon coating (a-C:H)	15	140	2.8	0.2	1.1	0.32	2.0
Bulk graphite (for comparison)	Very soft	9–15	–	–	–	–	–
Diamond (for comparison)	80–104	900–1,050	–	–	–	–	–
Si(100) substrate	11	220	0.75	–	0.6	0.55	0.02

[a]Measured on 100 nm thick coatings
[b]Measured on 20 nm thick coatings
[c]Measured on 400 nm thick coatings
[d]N_f was obtained for a mean load of 10 μN and a load amplitude of 8 μN

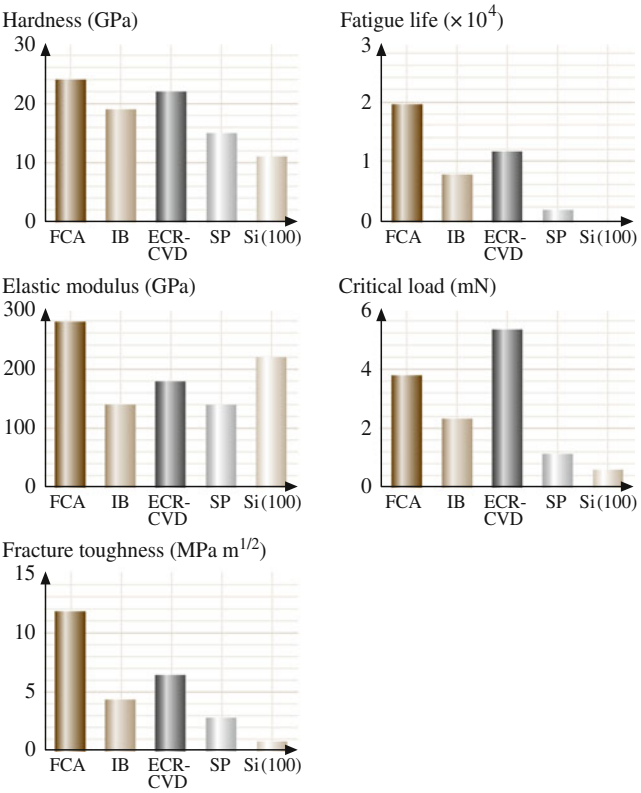

Fig. 17.10 Bar charts summarizing data for various coatings and single-crystal silicon substrate. Hardnesses, elastic moduli, and fracture toughnesses were measured on 100 nm thick coatings, and fatigue lifetimes and critical loads during scratch were measured on 20 nm thick coatings

Bell [94] reported an increase in hardness from 12 to 30 GPa and an increase in elastic modulus from 62 to 213 GPa with an increase in the sp^3-to-sp^2 bonding ratio, from 3 to 6, for a C:H coating deposited by low-energy ion-assisted unbalanced magnetron sputtering of a graphite target in an Ar–H_2 mixture.

Bhushan et al. [35] reported hardnesses of about 15 and 35 GPa and elastic moduli of about 140 and 200 GPa, measured by nanoindentation, for a-C:H coatings deposited by DC magnetron sputtering and RF-plasma-enhanced chemical vapor deposition techniques, respectively. The high hardness of RF-PECVD a-C:H coatings is attributed to a higher concentration of sp^3 bonding than in a sputtered hydrogenated a-C:H coating. Hydrogen is believed to play a crucial role in the bonding configuration of carbon atoms by helping to stabilize the tetrahedral coordination (sp^3 bonding) of carbon species. Jansen et al. [78] suggested that the incorporation of hydrogen efficiently passivates the dangling bonds and saturates the graphitic bonding to some extent. However, a large concentration of hydrogen in the plasma in sputter deposition is undesirable. Cho et al. [33] and

Rubin et al. [40] observed that the hardness decreased from 15 to 3 GPa with increased hydrogen content. Bhushan and Doerner [95] reported a hardness of about 10–20 GPa and an elastic modulus of about 170 GPa, measured by nanoindentation, for 100 nm thick DC magnetron sputtered a-C:H on the silicon substrate.

Residual stresses measured using a well-known curvature measurement technique are also presented in Table 17.5. The DLC coatings are under significant compressive internal stresses. Very high compressive stresses in FCA coatings are believed to be partly responsible for their high hardness. However, high stresses result in coating delamination and buckling. For this reason, the coatings that are thicker than about 1 μm have a tendency to delaminate from the substrates.

Fracture Toughness

Representative load–displacement curves of indentations on 400 nm thick cathodic arc carbon coating on silicon for various peak loads are shown in Fig. 17.11. Steps are found in all of the curves, as shown by arrows in Fig. 17.11a. In the 30 mN SEM micrograph, in addition to several radial cracks, ring-like through-thickness cracking is observed with small lips of material overhanging the edge of indentation. The steps at about 23 mN in the loading curves of indentations made with 30 and 100 mN peak indentation loads result from the ring-like through-thickness cracking. The step at 175 mN in the loading curve of the indentation made with 200 mN peak indentation load is caused by spalling and second ring-like through-thickness cracking.

According to Li et al. [87], the fracture process progresses in three stages: (1) ring-like through-thickness cracks form around the indenter due to high stresses in the contact area, (2) delamination and buckling occur around the contact area at the coating–substrate interface due to high lateral pressure, and (3) second ring-like through-thickness cracks and spalling are generated by high bending stresses at the edges of the buckled coating (Fig. 17.12a). In the first stage, if the coating under the indenter is separated from the bulk coating via the first ring-like through-thickness cracking, a corresponding step will be present in the loading curve. If discontinuous cracks form and the coating under the indenter is not separated from the remaining coating, no step appears in the loading curve, because the coating still supports the indenter and the indenter cannot suddenly advance into the material. In the second stage, for the coating used in the present study, the advances of the indenter during the radial cracking delamination, and buckling are not big enough to form steps in the loading curve, because the coating around the indenter still supports the indenter, but they generate discontinuities that change the slope of the loading curve with increasing indentation load. In the third stage, the stress concentration at the end of the interfacial crack cannot be relaxed by the propagation of the interfacial crack. With an increase in indentation depth, the height of the bulged coating increases. When the height reaches a critical value, the bending stresses caused by the bulged coating around the indenter will result in second ring-like through-thickness crack formation and spalling at the edge of the buckled coating,

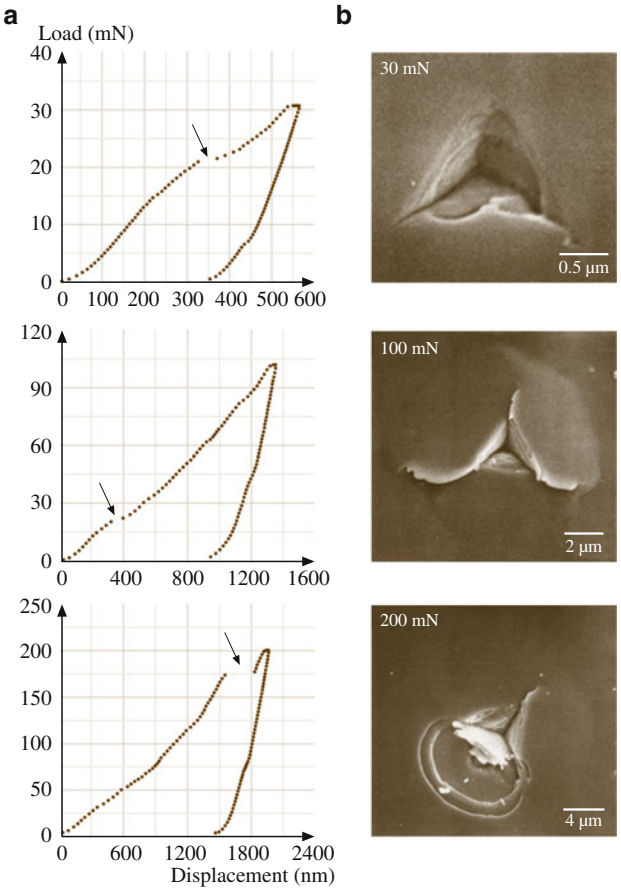

Fig. 17.11 **(a)** Load–displacement curves of indentations made with 30, 100, and 200 mN peak indentation loads using the cube corner indenter, and **(b)** SEM micrographs of indentations on a 400 nm thick cathodic arc carbon coating on silicon. *Arrows* indicate steps during the loading portion of the load–displacement curve [87]

as shown in Fig. 17.12a, which leads to a step in the loading curve. This is a single event and it results in the separation of the part of the coating around the indenter from the bulk coating via cracking through coatings. The step in the loading curve results (completely) from the coating cracking and not from the interfacial cracking or the substrate cracking.

The area under the load–displacement curve is the work performed by the indenter during the elastic–plastic deformation of the coating/substrate system. The strain energy release in the first/second ring-like cracking and spalling can be calculated from the corresponding steps in the loading curve. Figure 17.12b shows a modeled load–displacement curve. 0ACD is the loading curve and DE is the unloading curve. The first ring-like through-thickness crack should be considered.

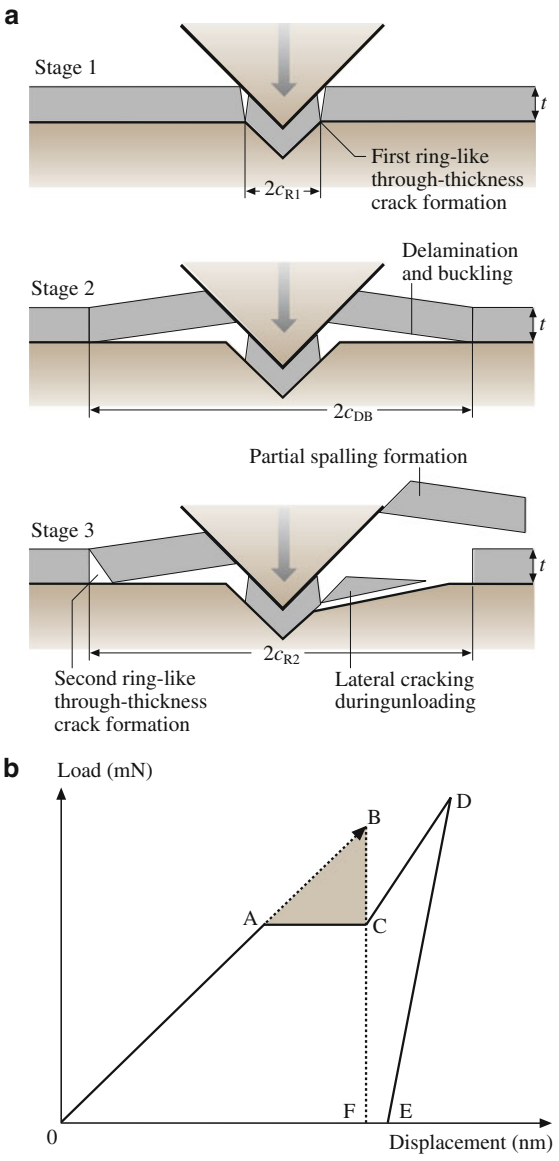

Fig. 17.12 **(a)** Schematic of various stages in nanoindentation fracture for the coating/substrate system, and **(b)** schematic of a load–displacement curve showing a step during the loading cycle and the associated energy release

It should be emphasized that the edge of the buckled coating is far from the indenter and, therefore, it does not matter if the indentation depth exceeds the coating thickness, or if deformation of the substrate occurs around the indenter when we measure the fracture toughness of the coating from the energy released during the second ring-like through-thickness cracking (spalling). Suppose that the second ring-like through-thickness cracking occurs at AC. Now, let us consider the loading curve 0AC. If the second ring-like through-thickness crack does not occur, 0A will

extend to 0B to reach the same displacement as 0C. This means that crack formation changes the loading curve 0AB into 0AC. For point B, the elastic–plastic energy stored in the coating/substrate system should be 0BF. For point C, the elastic–plastic energy stored in the coating/substrate system should be 0ACF. Therefore, the energy difference before and after the crack generation is the area of ABC, so this energy stored in ABC will be released as strain energy, creating the ring-like through-thickness crack. According to the theoretical analysis by Li et al. [87], the fracture toughness of a thin film can be written as

$$K_{\mathrm{Ic}} = \left[\left(\frac{E}{(1-\nu^2)2\pi C_R}\right)\left(\frac{U}{t}\right)\right]^{1/2}, \tag{17.2}$$

where E is the elastic modulus, ν is the Poisson ratio, $2\pi C_{\mathrm{R}}$ is the crack length in the coating plane, t is the coating thickness, and U is the strain energy difference before and after cracking.

The fracture toughness of the coatings can be calculated using (17.2). The loading curve is extrapolated along the tangential direction of the loading curve from the starting point of the step up to reach the same displacement as the step. The area between the extrapolated line and the step is the estimated strain energy difference before and after cracking. C_{R} is measured from SEM micrographs or AFM images of indentations. The second ring-like crack is where the spalling occurs. For example, for the 400 nm thick cathodic arc carbon coating data presented in Fig. 17.11, the U value of 7.1 nN m is assessed from the steps in Fig. 17.11a at peak indentation loads of 200 mN. For a C_{R} value of 7.0 μm, from Fig. 17.11b, with E =300 GPa (measured using a nanoindenter and an assumed value of 0.25 for ν), fracture toughness values are calculated as 10.9 MPa $\sqrt{\mathrm{m}}$ [87, 88]. The fracture toughness and related data for various 100 nm thick DLC coatings are presented in Fig. 17.10 and Table 17.5.

Nanofatigue

Delayed fracture resulting from extended service is called fatigue [96]. Fatigue fracturing progresses through a material via changes within the material at the tip of a crack, where there is a high stress intensity. There are several situations: cyclic fatigue, stress corrosion and static fatigue. Cyclic fatigue results from cyclic loading of machine components. In a low-flying slider in a magnetic head-disk interface, isolated asperity contacts occur during use and the fatigue failure occurs in the multilayered thin film structure of the magnetic disk [13]. Impact occurs in many MEMS components and the failure mode is cyclic fatigue. Asperity contacts can be simulated using a sharp diamond tip in oscillating contact with the component.

Figure 17.13 shows the schematic of a fatigue test on a coating/substrate system using a continuous stiffness measurement (CSM) technique. Load cycles are applied to the coating, resulting in cyclic stress. P is the cyclic load, P_{mean} is the

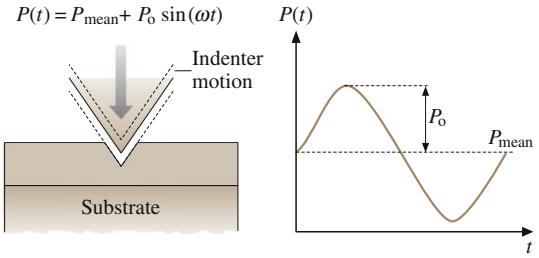

Fig. 17.13 Schematic of a fatigue test on a coating/substrate system using the continuous stiffness measurement technique

mean load, P_o is the oscillation load amplitude, and ω is the oscillation frequency. The following results can be obtained: (1) endurance limit (the maximum load below which there is no coating failure for a preset number of cycles); (2) number of cycles at which the coating failure occurs; and (3) changes in contact stiffness (measured using the unloading slope of each cycle), which can be used to monitor the propagation of interfacial cracks during a cyclic fatigue process.

Figure 17.14a shows the contact stiffness as a function of the number of cycles for 20 nm thick FCA coatings cyclically deformed by various oscillation load amplitudes with a mean load of 10 μN at a frequency of 45 Hz. At 4 μN load amplitude, no change in contact stiffness was found for all coatings. This indicates that 4 μN load amplitude is not high enough to damage the coatings. At 6 μN load amplitude, an abrupt decrease in contact stiffness was found after a certain number of cycles for each coating, indicating that fatigue damage had occurred. With increasing load amplitude, the number of cycles to failure N_f decreases for all coatings. Load amplitude versus N_f, a so-called S–N curve, is plotted in Fig. 17.14b. The critical load amplitude below which no fatigue damage occurs (an endurance limit), was identified for each coating. This critical load amplitude, together with the mean load, are of critical importance to the design of head-disk interfaces or MEMS/NEMS device interfaces.

To compare the fatigue lives of the different coatings studied, the contact stiffness is shown as a function of the number of cycles for 20 nm thick FCA, IB, ECR-CVD and SP coatings cyclically deformed by an oscillation load amplitude of 8 μN with a mean load of 10 μN at a frequency of 45 Hz in Fig. 17.14c. The FCA coating has the largest N_f, followed by the ECR-CVD, IB and SP coatings. In addition, after N_f, the contact stiffness of the FCA coating shows a slower decrease than the other coatings. This indicates that the FCA coating was less damaged than the others after N_f. The fatigue behaviors of FCA and ECR-CVD coatings of different thicknesses are compared in Fig. 17.14d. For both coatings, N_f decreases with decreasing coating thickness. At 10 nm, FCA and ECR-CVD have almost the same fatigue life. At 5 nm, the ECR-CVD coating shows a slightly longer fatigue life than the FCA coating. This indicates that the microstructure and residual stresses are not uniform across the thickness direction, even for nanometer-thick DLC coatings. Thinner coatings are more influenced by interfacial stresses than thicker coatings.

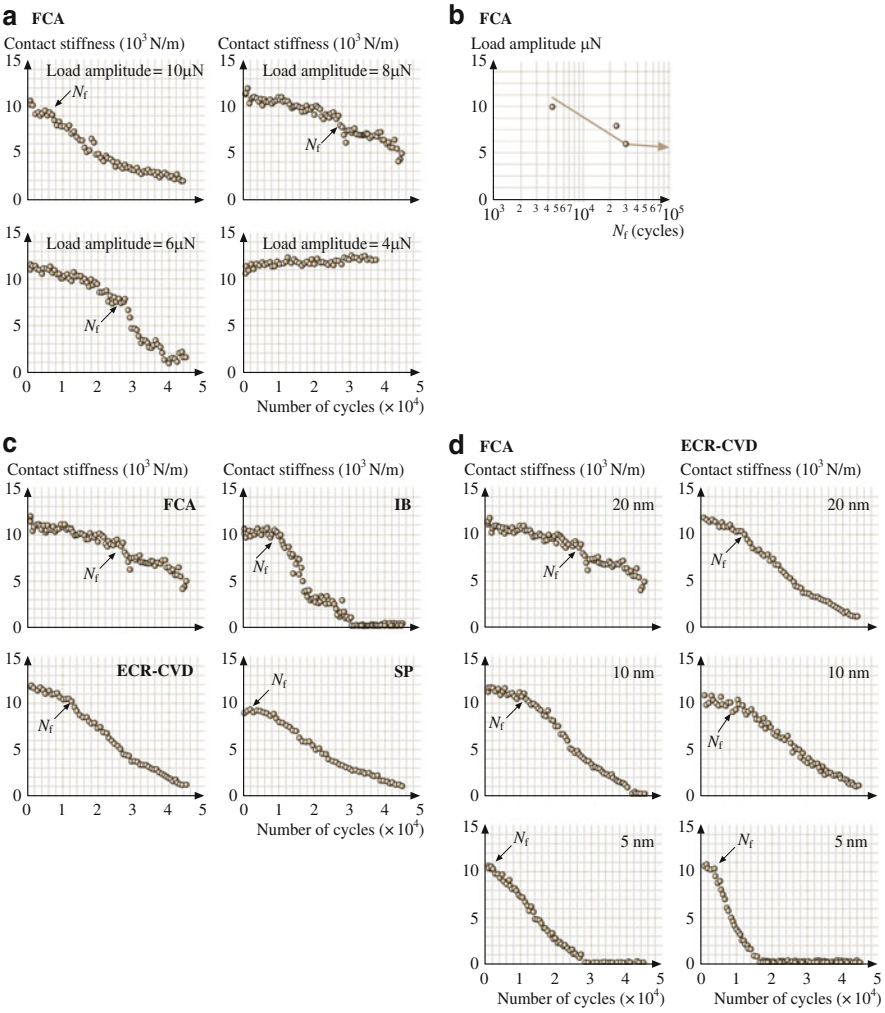

Fig. 17.14 **(a)** Contact stiffness as a function of the number of cycles for 20 nm thick FCA coatings cyclically deformed by various oscillation load amplitudes with a mean load of 10 μN at a frequency of 45 Hz; **(b)** plot of load amplitude versus N_f; **(c)** contact stiffness as a function of the number of cycles for four different 20 nm thick coatings with a mean load of 10 μN and a load amplitude of 8 μN at a frequency of 45 Hz; and **(d)** contact stiffness as a function of the number of cycles for two coatings of different thicknesses at a mean load of 10 μN and a load amplitude of 8 μN at a frequency of 45 Hz

Figure 17.15a shows high-magnification SEM images of 20 nm thick FCA coatings before, at, and after N_f. In the SEM images, the net-like structure is the gold film coated on the DLC coating, which should be ignored when analyzing the indentation fatigue damage. Before N_f, no delamination or buckling was found except for the residual indentation mark at magnifications of up to 1,200,000 × using SEM.

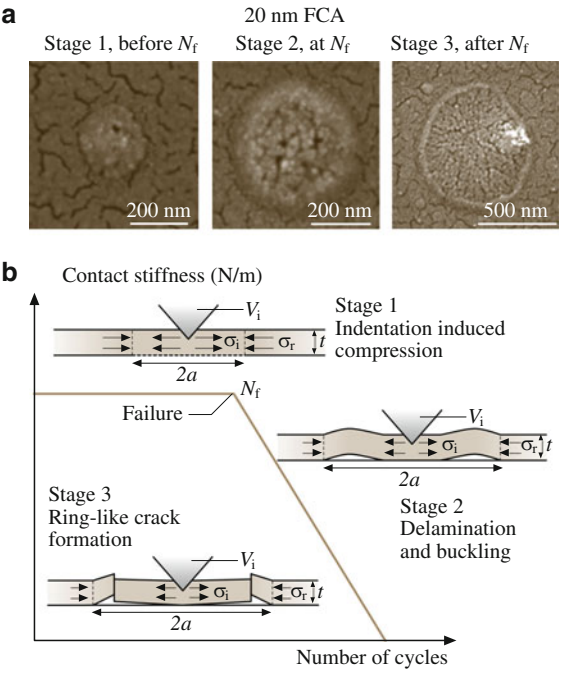

Fig. 17.15 **(a)** High-magnification SEM images of a coating before, at, and after N_f, and **(b)** schematic of various stages of indentation fatigue damage for a coating/substrate system [90]

This suggests that only plastic deformation occurred before N_f. At N_f, the coating around the indenter bulged upwards, indicating delamination and buckling. Therefore, it is believed that the decrease in contact stiffness at N_f results from delamination and buckling of the coating from the substrate. After N_f, the buckled coating was broken down around the edge of the buckled area, forming a ring-like crack. The remaining coating overhung at the edge of the buckled area. It is noted that the indentation size increases with the number of cycles. This indicates that deformation, delamination and buckling as well as ring-like crack formation occurred over a period of time.

The schematic in Fig. 17.15b shows various stages of indentation fatigue damage for a coating/substrate system. Based on this study, three stages of indentation fatigue damage appear to exist: (1) indentation-induced compression; (2) delamination and buckling; (3) ring-like crack formation at the edge of the buckled coating. The deposition process often induces residual stresses in coatings. The model shown in Fig. 17.15b considers a coating with uniform biaxial residual compression σ_r. In the first stage, indentation induces elastic/plastic deformation, exerting a pressure (acting outward) on the coating around the indenter. Interfacial defects like voids and impurities act as original cracks. These cracks propagate and link up as the indentation compressive stress increases. At this stage, the coating, which is under the indenter and above the interfacial crack (with a crack length of $2a$), still maintains a solid contact with the substrate; the substrate still fully supports the coating. Therefore, this interfacial crack does not lead to an abrupt

decrease in contact stiffness, but gives rise to a slight decrease in contact stiffness, as shown in Fig. 17.14. The coating above the interfacial crack is treated as a rigidly clamped disk. We assume that the crack radius a is large compared with the coating thickness t. Since the coating thickness ranges from 5 to 20 nm, this assumption is easily satisfied in this study (the radius of the delaminated and buckled area, shown in Fig. 17.15a, is on the order of 100 nm). The compressive stress caused by indentation is given as [97]

$$\sigma_{\mathrm{i}} = \frac{E}{(1-v)}\varepsilon_{\mathrm{i}} = \frac{EV_{\mathrm{i}}}{2\pi t a^2(1-v)}, \tag{17.3}$$

where ν and E are the Poisson ratio and elastic modulus of the coating, V_{i} is the indentation volume, t is the coating thickness, and a is the crack radius. As the number of cycles increases, so does the indentation volume V_{i}. Therefore, the indentation compressive stress σ_{i} increases accordingly. In the second stage, buckling occurs during the unloading segment of the fatigue testing cycle when the sum of the indentation compressive stress σ_{i} and the residual stress σ_{r} exceed the critical buckling stress σ_{b} for the delaminated circular section, as given by [98]

$$\sigma_{\mathrm{b}} = \frac{\mu^2 E}{12(1-v^2)}\left(\frac{t}{a}\right)^2, \tag{17.4}$$

where the constant μ equals 42.67 for a circular clamped plate with a constrained center point and 14.68 when the center is unconstrained. The buckled coating acts as a cantilever. In this case, the indenter indents a cantilever rather than a coating/substrate system. This ultrathin coating cantilever has much less contact stiffness than the coating/substrate system. Therefore, the contact stiffness shows an abrupt decrease at N_{f}. In the third stage, with more cycles, the delaminated and buckled size increases, resulting in a further decrease in contact stiffness since the cantilever beam length increases. On the other hand, a high bending stress acts at the edge of the buckled coating. The larger the buckled size, the higher the bending stress. The cyclic bending stress causes fatigue damage at the end of the buckled coating, forming a ring-like crack. The coating under the indenter is separated from the bulk coating (caused by the ring-like crack at the edge of the buckled coating) and the substrate (caused by the delamination and buckling in the second stage). Therefore, the coating under the indenter is not constrained; it is free to move with the indenter during fatigue testing. At this point, the sharp nature of the indenter is lost, because the coating under the indenter gets stuck on the indenter. The indentation fatigue experiment results in the contact of a (relatively) huge blunt tip with the substrate. This results in a low contact stiffness value.

Compressive residual stresses result in delamination and buckling. A coating with a higher adhesion strength and a lower compressive residual stress is required for a higher fatigue life. Interfacial defects should be avoided in the coating deposition process. We know that ring-like crack formation occurs in the coating.

Formation of fatigue cracks in the coating depends upon the hardness and the fracture toughness. Cracks are more difficult to form and propagate in the coating with higher strength and fracture toughness.

It is now accepted that long fatigue life in a coating/substrate almost always involves *living with a crack*, that the threshold or limit condition is associated with the nonpropagation of existing cracks or defects, even though these cracks may be undetectable [96]. For all of the coatings studied at 4 μN, the contact stiffness does not change much. This indicates that delamination and buckling did not occur within the number of cycles tested in this study. This is probably because the indentation-induced compressive stress was not high enough to allow the cracks to propagate and link up under the indenter, or the sum of the indentation compressive stress σ_i and the residual stress σ_r did not exceed the critical buckling stress σ_b.

Figure 17.10 and Table 17.5 summarize the hardnesses, elastic moduli, fracture toughnesses, and fatigue lifetimes of all of the coatings studied. A good correlation exists between the fatigue life and other mechanical properties. Higher mechanical properties result in a longer fatigue life. The mechanical properties of DLC coatings are controlled by the sp^3-to-sp^2 ratio. An sp^3-bonded carbon exhibits the outstanding properties of diamond [51]. Higher kinetic energy during deposition will result in a larger fraction of sp^3-bonded carbon in an amorphous network. Thus, the higher kinetic energy for the FCA could be responsible for its enhanced carbon structure and mechanical properties [48–50, 99]. Higher adhesion strength between the FCA coating and substrate makes the FCA coating more difficult to delaminate from the substrate.

17.3.2 Microscratch and Microwear Studies

For microscratch studies, a conical diamond indenter (that has a tip radius of about 1 μm and a cone angle of 60° for example) is drawn over the sample surface, and the load is ramped up (typically from 2 to 25 mN) until substantial damage occurs. The coefficient of friction is monitored during scratching. Scratch-induced coating damage, specifically fracture or delamination, can be monitored by in situ friction force measurements and using optical and SEM imaging of the scratches after tests. A gradual increase in friction is associated with plowing, and an abrupt increase in friction is associated with fracture or catastrophic failure [100]. The load corresponding to an abrupt increase in friction or an increase in friction above a certain value (typically 2 × the initial value) provides a measure of the scratch resistance or the adhesive strength of a coating, and is called the *critical load*. The depths of scratches are measured with increasing scratch length or normal load using an AFM, typically with an area of $10 \times 10\ \mu m^2$ [48, 49, 101].

Microscratch and microwear studies are also conducted using an AFM [23, 50, 99, 102, 103]. A square pyramidal diamond tip (tip radius ≈ 100 nm) or a three-sided pyramidal diamond (Berkovich) tip with an apex angle of 60° and a tip radius of about 100 nm, mounted on a platinum-coated, rectangular stainless steel

cantilever of stiffness of about 40 N/m, is scanned orthogonal to the long axis of the cantilever to generate scratch and wear marks. During the scratch test, the normal load is either kept constant or is increased (typically from 0 to 100 μN) until damage occurs. Topographical images of the scratch are obtained in situ with the AFM at a low load. By scanning the sample during scratching, wear experiments can be conducted. Wear is monitored as a function of the number of cycles at a constant load. Normal loads (10–80 μN) are typically used.

Microscratch

Scratch tests conducted with a sharp diamond tip simulate a sharp asperity contact. In a scratch test, the cracking or delamination of a hard coating is signaled by a sudden increase in the coefficient of friction [23]. The load associated with this event is called the *critical load*.

Wu [104], Bhushan et al. [70], Gupta and Bhushan [12,47], and Li and Bhushan [48, 49, 101] have used a nanoindenter to perform microscratch (mechanical durability) studies of various carbon coatings. The coefficient of friction profiles as a function of increasing normal load as well as AFM surface height maps of regions over scratches at the respective critical loads (indicated by the arrows in the friction profiles and AFM images) observed for coatings with different thicknesses and single-crystal silicon substrate using a conical tip are compared in Figs. 17.16 and 17.17. Bhushan and Koinkar [102], Koinkar and Bhushan [103], Bhushan [23], and Sundararajan and Bhushan [50, 99] used an AFM to perform microscratch studies. Data obtained for coatings with different thicknesses and silicon substrate using a Berkovich tip are compared in Figs. 17.18 and 17.19. Critical loads for various coatings tested using a nanoindenter and AFM are summarized in Fig. 17.20. Selected data for 20 nm thick coatings obtained using nanoindenter are also presented in Fig. 17.10 and Table 17.5.

It is clear that a well-defined critical load exists for each coating. The AFM images clearly show that below the critical loads the coatings were plowed by the scratch tip, associated with the plastic flow of materials. At and after the critical loads, debris (chips) or buckling was observed on the sides of the scratches. Delamination or buckling can be observed around or after the critical loads, which suggests that the damage starts from delamination and buckling. For the 3.5 and 5 nm thick FCA coatings, before the critical loads small debris is observed on the sides of the scratches. This suggests that the thinner FCA coatings are not so durable. It is obvious that, for a given deposition method, the critical loads increase with increasing coating thickness. This indicates that the critical load is determined not only by the strength of adhesion to the substrate, but also by the coating thickness. We note that more debris generated on the thicker coatings than thinner coatings. A thicker coating is more difficult to break; the broken coating chips (debris) seen for a thicker coating are larger than those for the thinner coatings. The different residual stresses of coatings of different thicknesses may also affect the size of the debris. The AFM image shows that the silicon substrate was damaged by

plowing, associated with the plastic flow of material. At and after the critical load, a small amount of uniform debris is observed and the amount of debris increases with increasing normal load.

Since the damage mechanism at the critical load appears to be the onset of plowing, harder coatings with more fracture toughness will therefore require a higher load for deformation and hence a higher critical load. Figure 17.21 gives critical loads of various coatings, obtained with AFM tests, as a function of the coating hardness and fracture toughness (from Table 17.5). It can be seen that, in general, increasing coating hardness and fracture toughness results in a higher critical load. The only exceptions are the FCA coatings at 5 and 3.5 nm thickness, which show the lowest critical loads despite their high hardness and fracture toughness. The brittleness of the thinner FCA coatings may be one reason for their low critical loads. The mechanical properties of coatings that are less than 10 nm thick are not known. The FCA process may result in coatings with low hardness at low thickness due to differences in coating stoichiometry and structure compared to coatings of higher thickness. Also, at these thicknesses stresses at the coating–substrate interface may affect coating adhesion and load-carrying capacity.

Based on the experimental results, a schematic of the scratch damage mechanisms encountered for the DLC coatings used in this study is shown in Fig. 17.22.

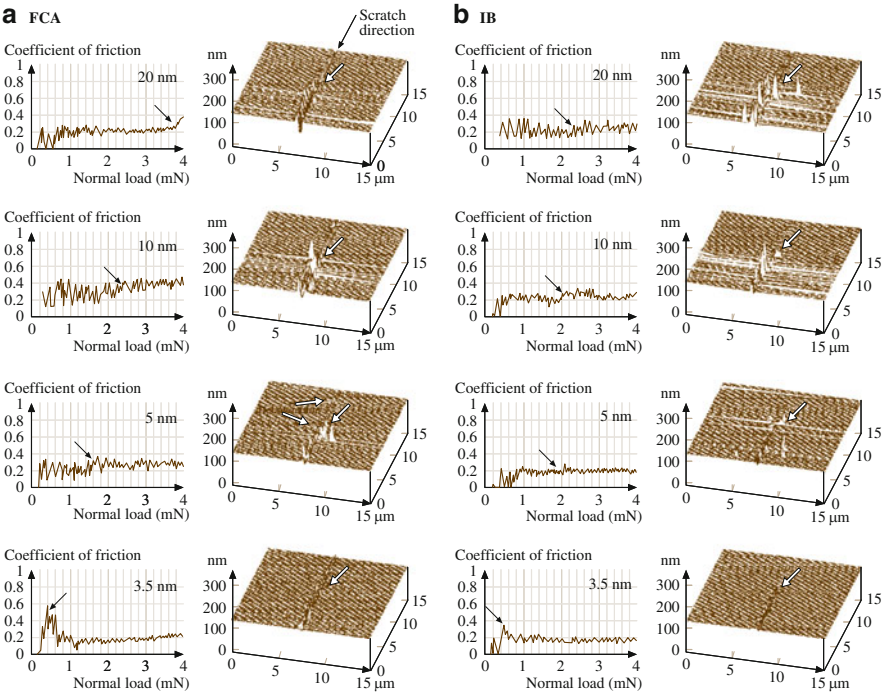

Fig. 17.16 (continued)

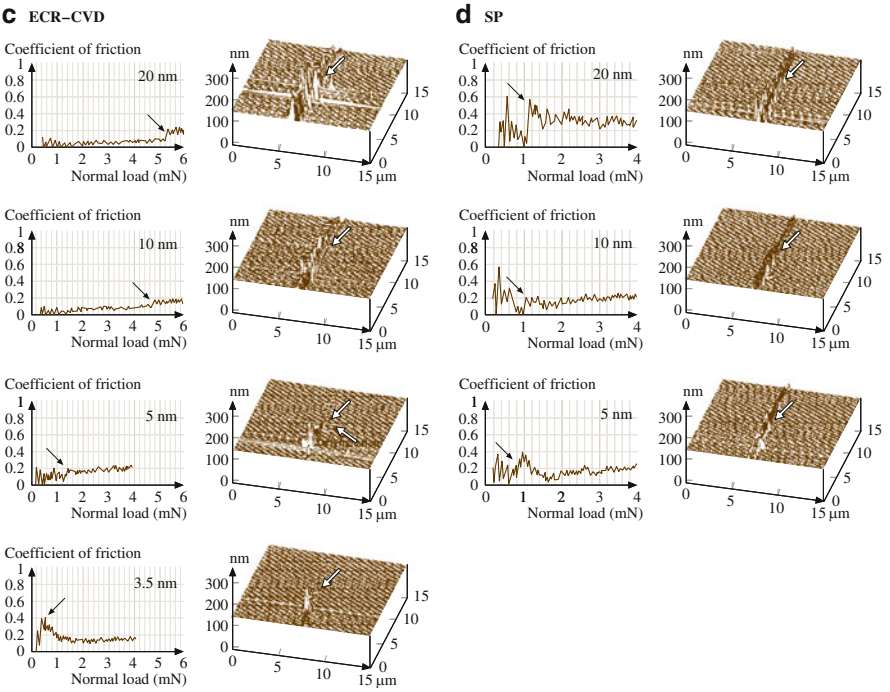

Fig. 17.16 Coefficient of friction profiles as a function of normal load, as well as corresponding AFM surface height maps of regions over scratches at the respective critical loads (indicated by the *arrows* in the friction profiles and AFM images), for coatings of different thicknesses deposited by various deposition techniques: **(a)** FCA, **(b)** IB, **(c)** ECR-CVD, **(d)** SP

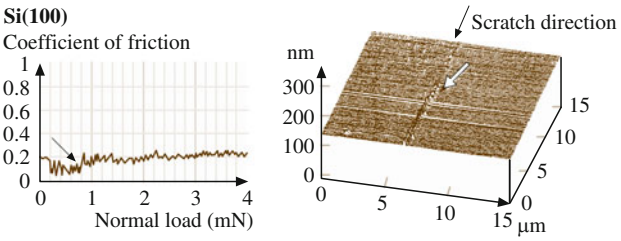

Fig. 17.17 Coefficient of friction profiles as a function of normal load as well as corresponding AFM surface height maps of regions over scratches at the respective critical loads (indicated by the *arrows* in the friction profiles and AFM images) for Si(100)

Below the critical load, if a coating has a good combination of strength and fracture toughness, plowing associated with the plastic flow of materials is responsible for the coating damage (Fig. 17.22a). However, if the coating has a low fracture toughness, cracking could occur during plowing, resulting in the formation of

small amounts of debris (Fig. 17.22b). When the normal load is increased to the critical load, delamination or buckling will occur at the coating–substrate interface (Fig. 17.22c). A further increase in normal load will result in coating breakdown via through-coating thickness cracking, as shown in Fig. 17.22d. Therefore, adhesion strength plays a crucial role in the determination of critical load. If a coating adheres strongly to the substrate, the coating is more difficult to delaminate, which will result in a higher critical load. The interfacial and residual stresses of a coating may also greatly affect the delamination and buckling [1]. A coating with higher interfacial and residual stresses is more easily delaminated and buckled, which will result in a low critical load. It was reported earlier that FCA coatings have higher residual stresses than other coatings [47]. Interfacial stresses play an increasingly important role as the coating gets thinner. A large mismatch in elastic modulus between the FCA coating and the silicon substrate may cause large interfacial stresses. This may be why thinner FCA coatings show lower critical loads than thicker FCA coatings, even though the FCA coatings have higher hardness and elastic moduli. The brittleness of thinner FCA coatings may be another reason for the lower critical loads. The strength and fracture toughness of a coating also affect the critical load. Greater strength and fracture toughness will make the coating more difficult to break after delamination and buckling. The high scratch resistance/adhesion of FCA coatings is attributed to the atomic intermixing that occurs at the coating–substrate interface due to the high kinetic energy (2 keV) of the plasma formed during the cathodic arc deposition process [57]. This atomic intermixing provides a graded compositional transition between the coating and the

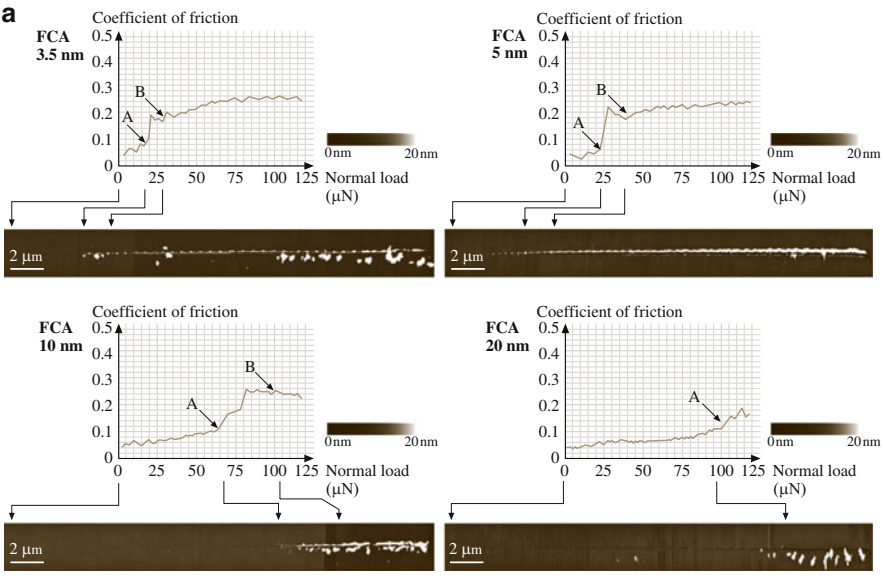

Fig. 17.18 (continued)

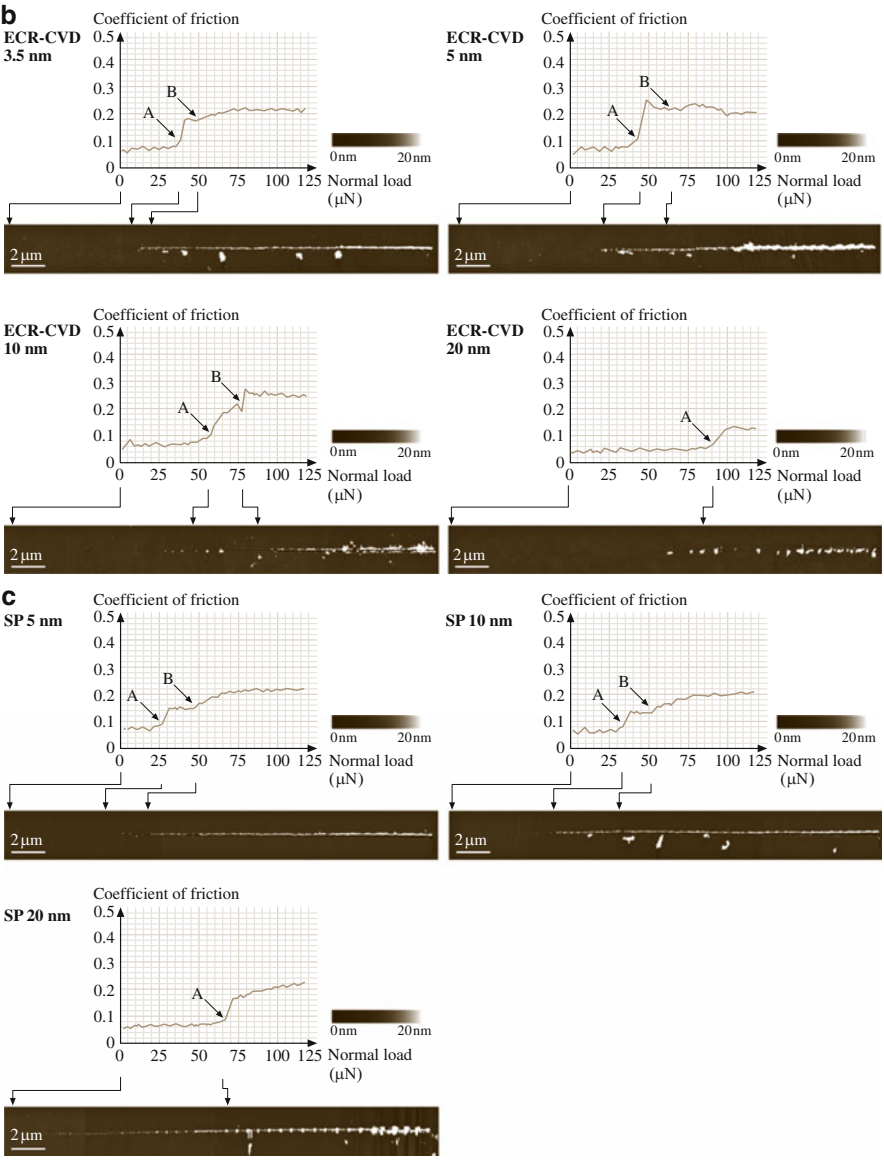

Fig. 17.18 Coefficient of friction profiles during scratch as a function of normal load and corresponding AFM surface height maps for **(a)** FCA, **(b)** ECR-CVD, and **(c)** SP coatings [99]

substrate material. In all other coatings used in this study, the kinetic energy of the plasma is insufficient for atomic intermixing.

Gupta and Bhushan [12, 47] and Li and Bhushan [48, 49] measured the scratch resistances of DLC coatings deposited on Al_2O_3-TiC, Ni-Zn ferrite and single-crystal

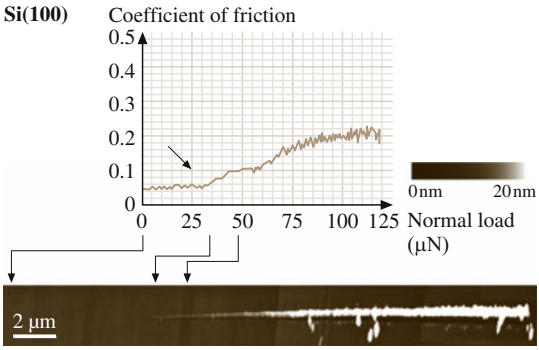

Fig. 17.19 Coefficient of friction profiles during scratch as a function of normal load and corresponding AFM surface height maps for Si(100) [99]

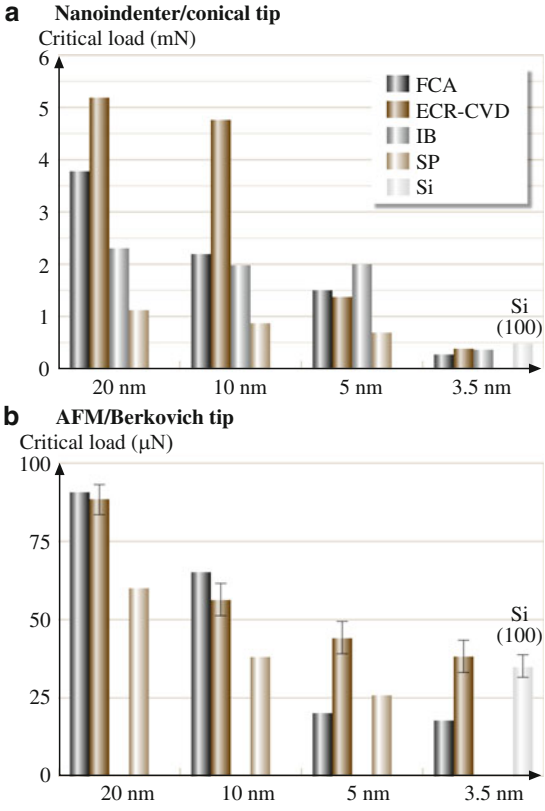

Fig. 17.20 Critical loads estimated from the coefficient of friction profiles from **(a)** nanoindenter and **(b)** AFM tests for various coatings of different thicknesses and Si(100) substrate

silicon substrates. An interlayer of silicon is required to adhere the DLC coating to other substrates, except in the case of cathodic arc-deposited coatings. The best adhesion with cathodic arc carbon coating is obtained on electrically conducting substrates such as Al_2O_3-TiC and silicon rather than Ni–Zn ferrite.

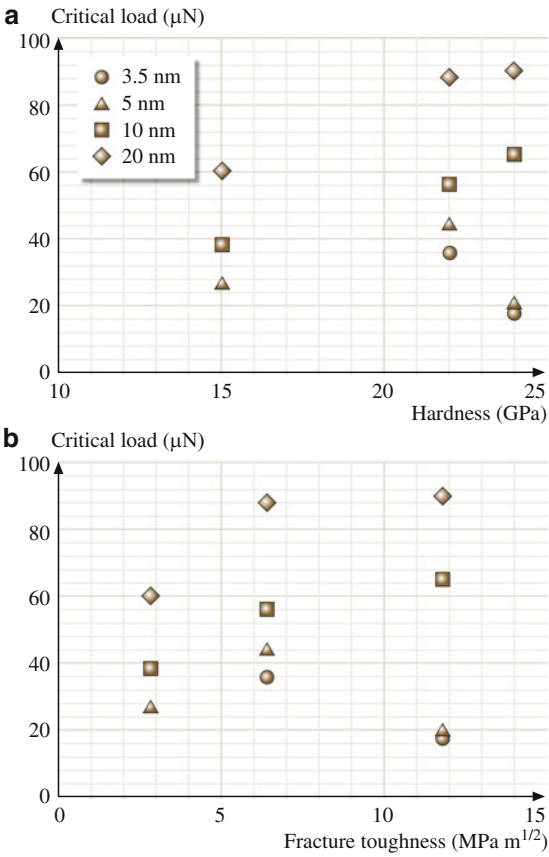

Fig. 17.21 Measured critical loads estimated from the coefficient of friction profiles from AFM tests as a function of **(a)** coating hardness and **(b)** fracture toughness. Coating hardness and fracture toughness values were obtained using a nanoindenter on 100 nm thick coatings (Table 17.5)

Microwear

Microwear studies can be conducted using an AFM [23]. For microwear studies, a three-sided pyramidal single-crystal natural diamond tip with an apex angle of about 80° and a tip radius of about 100 nm is used at relatively high loads of 1–150 μN. The diamond tip is mounted on a stainless steel cantilever beam with a normal stiffness of about 30 N/m. The sample is generally scanned in a direction orthogonal to the long axis of the cantilever beam (typically at a rate of 0.5 Hz). The tip is mounted on the beam such that one of its edges is orthogonal to the beam axis. In wear studies, an area of 2×2 μm^2 is typically scanned for a selected number of cycles.

Microwear studies of various types of DLC coatings have been conducted [50, 102, 103]. Figure 17.23a shows a wear mark on uncoated Si(100). Wear occurs uniformly and material is removed layer-by-layer via plowing from the first cycle, resulting in constant friction force during the wear (Fig. 17.24a). Figure 17.23b shows AFM images of the wear marks on 10 nm thick coatings. It is clear that the

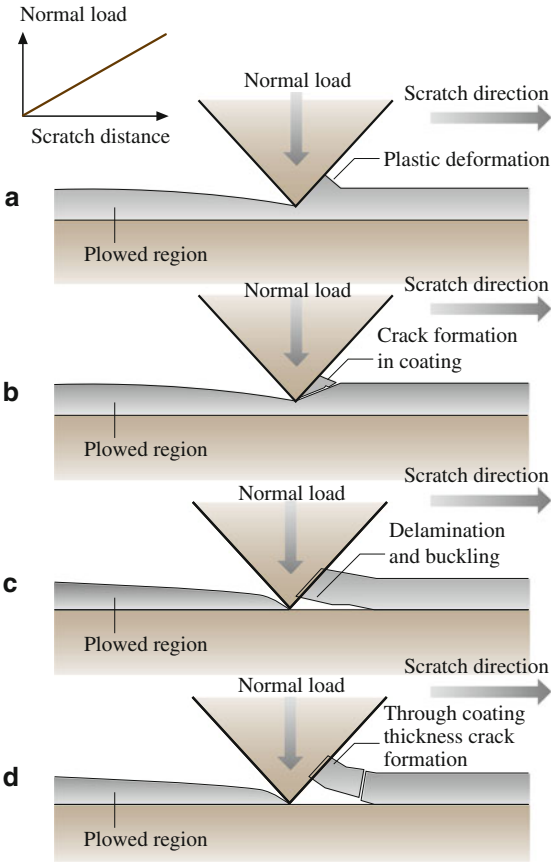

Fig. 17.22 Schematic of scratch damage mechanisms for DLC coatings: **(a)** plowing associated with the plastic flow of materials, **(b)** plowing associated with the formation of small debris, **(c)** delamination and buckling at the critical load, and **(d)** breakdown via through-coating thickness cracking at and after the critical load [48]

coatings wear nonuniformly. Coating failure is sudden and accompanied by a sudden rise in the friction force (Fig. 17.24b). Figure 17.24 shows the wear depth of Si(100) substrate and various DLC coatings at two different loads. FCA- and ECR-CVD-deposited 20 nm thick coatings show excellent wear resistance up to 80 μN, the load that is required for the IB 20 nm coating to fail. In these tests, *failure* of a coating occurs when the wear depth exceeds the quoted coating thickness. The SP 20 nm coating fails at a much lower load of 35 μN. At 60 μN, the coating hardly provides any protection. Moving on to the 10 nm coatings, the ECR-CVD coating requires about 45 cycles at 60 μN to fail, whereas the IB and FCA, coatings fail at 45 μN. The FCA coating exhibits slight roughening in the wear track after the first few cycles, which leads to an increase in the friction force. The SP coating continues to exhibit poor resistance, failing at 20 μN. For the 5 nm coatings, the load required to make the coatings fail continues to decrease, but IB and ECR-CVD still provide adequate protection compared to bare Si(100) in that order, with the silicon failing at 35 μN, the FCA coating at 25 μN and the SP coating at 20 μN. Almost all of the 20, 10, and 5 nm coatings provide better wear

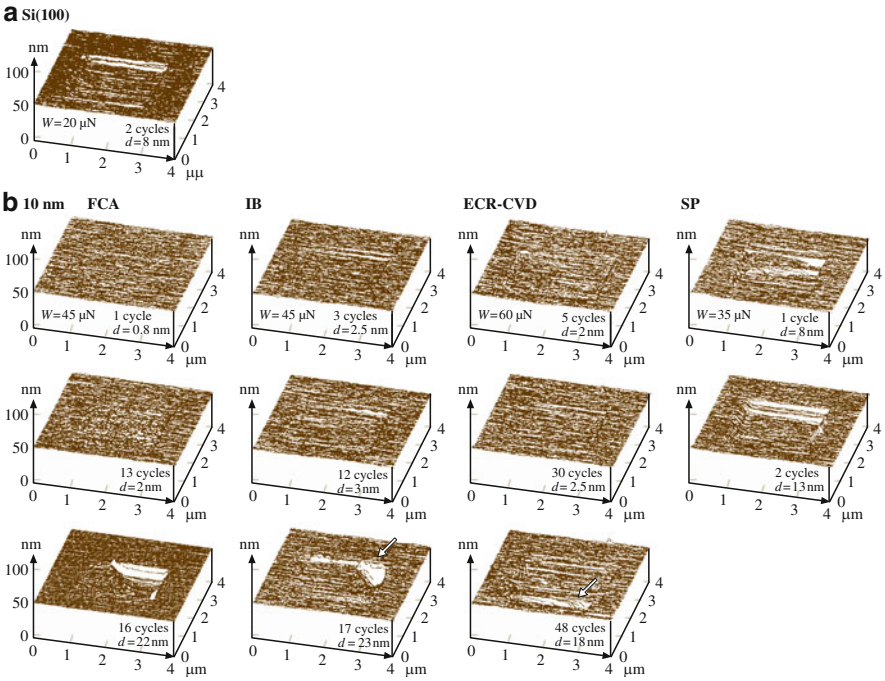

Fig. 17.23 AFM images of wear marks on **(a)** bare Si(100), and **(b)** various 10 nm thick DLC coatings [50]

resistance than bare silicon. At 3.5 nm, FCA coating provides no wear resistance, failing almost instantly at 20 μN. The IB and ECR-CVD coatings show good wear resistance at 20 μN compared to bare Si(100). However, IB only lasts about ten cycles and ECR-CVD about three cycles at 25 μN.

The wear tests highlight the differences between the coatings more vividly than the scratch tests. At higher thicknesses (10 and 20 nm), the ECR-CVD and FCA coatings appear to show the best wear resistance. This is probably due to the greater hardness of the coatings (Table 17.5). At 5 nm, the IB coating appears to be the best. FCA coatings show poorer wear resistance with decreasing coating thickness. This suggests that the trends in hardness seen in Table 17.5 no longer hold at low thicknesses. SP coatings show consistently poor wear resistance at all thicknesses. The 3.5 nm IB coating does provide reasonable wear protection at low loads.

17.3.3 Macroscale Tribological Characterization

So far, we have presented data on mechanical characterization and microscratch and microwear studies using a nanoindenter and an AFM. Mechanical properties affect the tribological performance of a coating, and microwear studies simulate a

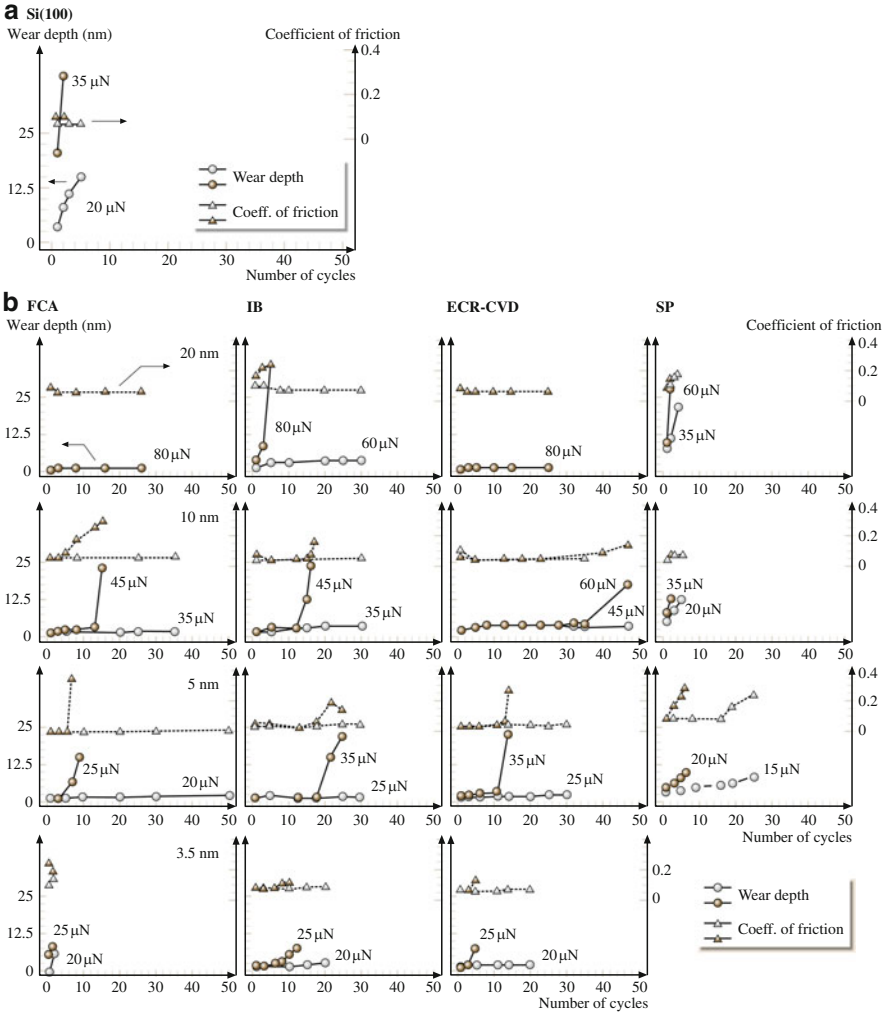

Fig. 17.24 Wear data for **(a)** bare Si(100) and **(b)** various DLC coatings. Coating thickness is constant along each row in **(b)**. Both the wear depth and the coefficient of friction during wear are plotted for a given cycle [50]

single asperity contact, which helps us to understand the wear process. These studies are useful when screening various candidate coatings, and also aid our understanding of the relationships between deposition conditions and properties of the samples. In the next step, macroscale friction and wear tests need to be conducted to measure the tribological performance of the coating.

Macroscale accelerated friction and wear tests have been conducted to screen a large number of candidates, as have functional tests on selected candidates. An accelerated test is designed to accelerate the wear process such that it does not

change the failure mechanism. The accelerated friction and wear tests are generally conducted using a ball-on-flat tribometer under reciprocating motion [70]. Typically, a diamond tip with a tip radius of 20 μm or a sapphire ball with a diameter of 3 mm and a surface finish of about 2 nm RMS is slid against the coated substrates at selected loads. The coefficient of friction is monitored during the tests.

Functional tests are conducted using an actual machine running at close to the actual operating conditions for which the coatings have been developed. The tests are generally accelerated somewhat to fail the interface in a short time.

Accelerated Friction and Wear Tests

Li and Bhushan [48] conducted accelerated friction and wear tests on DLC coatings deposited by various deposition techniques using a ball-on-flat tribometer. The average coefficient of friction values observed are presented in Table 17.5. Optical micrographs of wear tracks and debris formed on all samples when slid against a sapphire ball after a sliding distance of 5 nm are presented in Fig. 17.25. The normal load used for the 20 and 10 nm thick coatings was 200 mN, and the normal load used for the 5 and 3.5 nm thick coatings and the silicon substrate was 150 mN.

Among the 20 nm thick coatings, the SP coating exhibits a higher coefficient of friction (about 0.3) than for the other coatings coefficient of friction (all of which were about 0.2). The optical micrographs show that the SP coating has a larger wear track and more debris than the IB coating. No wear track or debris were found on the 20 nm thick FCA and ECR-CVD coatings. The optical micrographs of 10 nm thick coatings show that the SP coating was severely damaged, showing a large wear track with scratches and lots of debris. The FCA and ECR-CVD coatings show smaller wear tracks and less debris than the IB coatings.

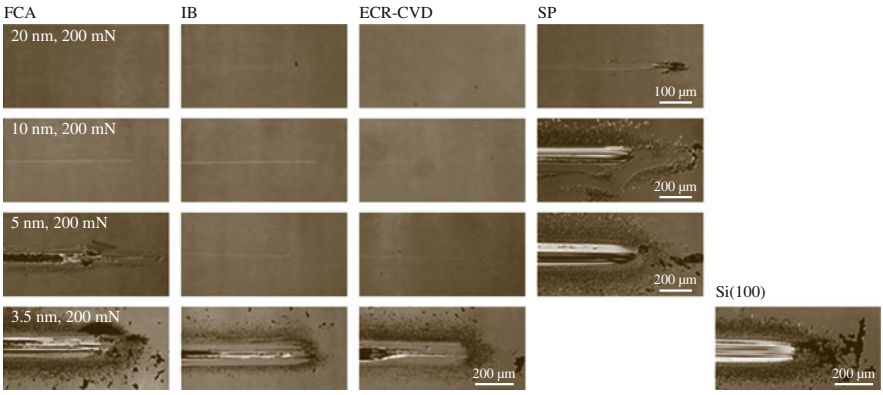

Fig. 17.25 Optical micrographs of wear tracks and debris formed on various coatings of different thicknesses and silicon substrate when slid against a sapphire ball after a sliding distance of 5 nm. The end of the wear track is on the right-hand side of the image

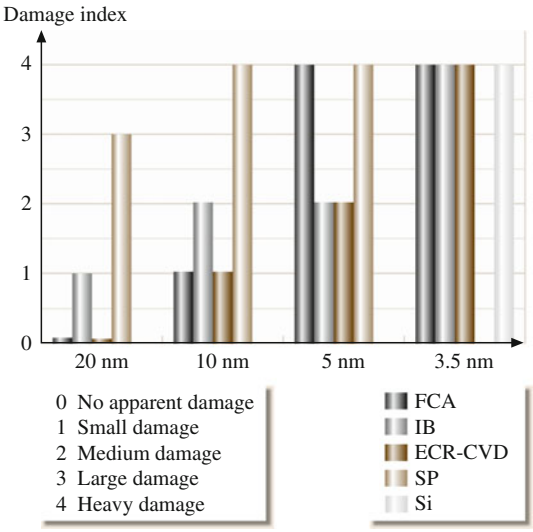

Fig. 17.26 Bar chart of the wear damage indices for various coatings of different thicknesses and Si(100) substrate based on optical examination of the wear tracks and debris

For the 5 nm thick coatings, the wear tracks and debris of the IB and ECR-CVD coatings are comparable. The bad wear resistance of the 5 nm thick FCA coating is in good agreement with the low critical scratch load, which may be due to the higher interfacial and residual stresses as well as the brittleness of the coating.

At 3.5 nm, all of the coatings exhibit wear. The FCA coating provides no wear resistance, failing instantly like the silicon substrate. Large block-like debris is observed on the sides of the wear track of the FCA coating. This indicates that large region delamination and buckling occurs during sliding, resulting in large block-like debris. This block-like debris, in turn, scratches the coating, making the damage to the coating even more severe. The IB and ECR-CVD coatings are able to provide some protection against wear at 3.5 nm.

In order to better evaluate the wear resistance of various coatings, based on an optical examination of the wear tracks and debris after tests, a bar chart of the wear damage index for various coatings of different thicknesses and an uncoated silicon substrate is presented in Fig. 17.26. Among the 20 and 10 nm thick coatings, the SP coatings show the worst damage, followed by FCA/ECR-CVD. At 5 nm, the FCA and SP coatings show the worst damage, followed by the IB and ECR-CVD coatings. All of the 3.5 nm thick coatings show the same heavy damage as the uncoated silicon substrate.

The wear damage mechanisms of the thick and thin DLC coatings studied are believed to be as illustrated in Fig. 17.27. In the early stages of sliding, deformation zone, Hertzian and wear fatigue cracks that have formed beneath the surface extend within the coating upon subsequent sliding [1]. Formation of fatigue cracks depends on the hardness and subsequent cycles. These are controlled by the sp^3-to-sp^2 ratio. For thicker coatings, the cracks generally do not penetrate the coating. For a thinner coating, the cracks easily propagate down to the interface aided by the interfacial

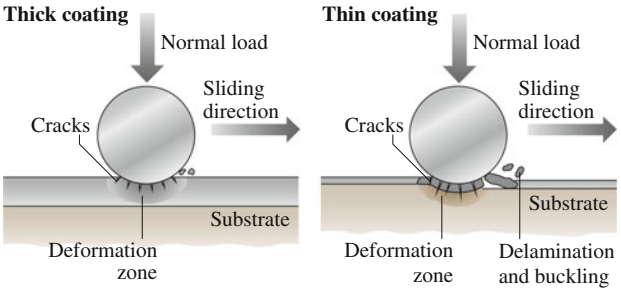

Fig. 17.27 Schematic of wear damage mechanisms for thick and thin DLC coatings [48]

stresses and get diverted along the interface just enough to cause local delamination of the coating. When this happens, the coating experiences excessive plowing. At this point, the coating fails catastrophically, resulting in a sudden rise in the coefficient of friction. All 3.5 nm thick coatings failed much quicker than the thicker coatings. It appears that these thin coatings have very low load-carrying capacities and so the substrate undergoes deformation almost immediately. This generates stresses at the interface that weaken the coating adhesion and lead to delamination of the coating. Another reason may be that the thickness is insufficient to produce a coating that has the DLC structure. Instead, the bulk may be made up of a matrix characteristic of the interface region where atomic mixing occurs with the substrate and/or any interlayer used. This would also result in poor wear resistance and silicon-like behavior of the coating, especially for FCA coatings, which show the worst performance at 3.5 nm. SP coatings show the worst wear performance at any thickness (Fig. 17.25). This may be due to their poor mechanical properties, such as lower hardness and scratch resistance, compared to the other coatings.

Comparison of Figs. 17.20 and 17.26 shows a very good correlation between the wear damage and critical scratch loads. Less wear damage corresponds to a higher critical scratch load. Based on the data, thicker coatings do show better scratch and wear resistance than thinner coatings. This is probably due to the better load-carrying capacities of the thick coatings compared to the thinner ones. For a given coating thickness, increased hardness and fracture toughness and better adhesion strength are believed to be responsible for the superior wear performance.

Effect of Environment

The friction and wear performance of an amorphous carbon coating is known to be strongly dependent on the water vapor content and partial gas pressure in the test environment. The friction data for an amorphous carbon film on a silicon substrate sliding against steel are presented as a function of the partial pressure of water vapor in Fig. 17.28 [1, 13, 69, 105, 106]. Friction increases dramatically above a relative humidity of about 40%. At high relative humidity, condensed water vapor forms

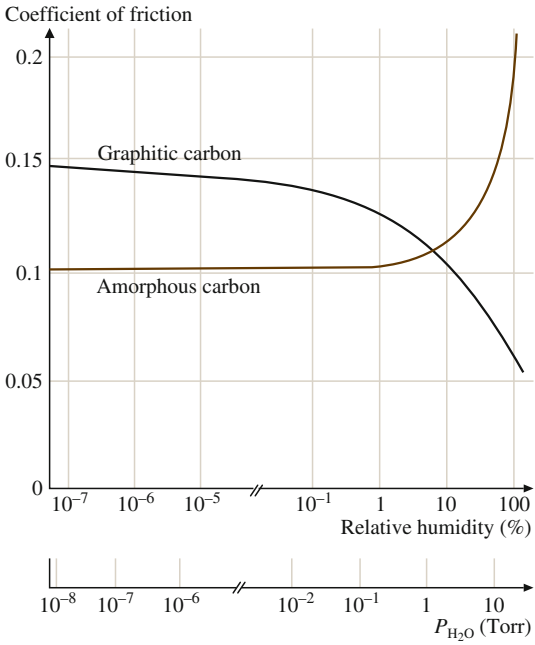

Fig. 17.28 Coefficient of friction as a function of relative humidity and water vapor partial pressure for a RF-plasma deposited amorphous carbon coating and a bulk graphitic carbon coating sliding against a steel ball

meniscus bridges at the contacting asperities, and the menisci result in an intrinsic attractive force that is responsible for an increase in the friction. For completeness, data on the coefficient of friction of bulk graphitic carbon are also presented in Fig. 17.28. Note that the friction decreases with increased relative humidity [107]. Graphitic carbon has a layered crystal lattice structure. Graphite absorbs polar gases (such as H_2O, O_2, CO_2, NH_3) at the edges of the crystallites, which weakens the interlayer bonding forces facilitating interlayer slip and results in lower friction [1].

A number of tests have been conducted in controlled environments in order to better study the effects of environmental factors on carbon-coated magnetic disks. Marchon et al. [108] conducted tests in alternating environments of oxygen and nitrogen gases (Fig. 17.29). The coefficient of friction increases as soon as oxygen is added to the test environment, whereas in a nitrogen environment the coefficient of friction reduces slightly. Tribochemical oxidation of the DLC coating in the oxidizing environment is responsible for an increase in the coefficient of friction, implying wear. Dugger et al. [109], Strom et al. [110], Bhushan and Ruan [111] and Bhushan et al. [71] conducted tests with DLC-coated magnetic disks (with about 2 nm thick perfluoropolyether lubricant film) in contact with Al_2O_3–TiC sliders in different gaseous environments, including a high vacuum of 2×10^{-7} Torr (Fig. 17.30). The wear lives are the shortest in high vacuum and the longest in atmospheres of mostly nitrogen and argon with the following order (from best to worst): argon or nitrogen, Ar + H_2O, ambient, Ar + O_2, Ar + H_2O, vacuum. From this sequence of wear performance, we can see that having oxygen and water in an operating environment worsens the wear performance of the coating, but having a

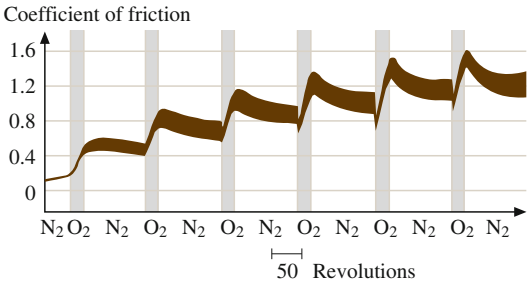

Fig. 17.29 Coefficient of friction as a function of sliding distance for a ceramic slider against a magnetic disk coated with a 20 nm thick DC magnetron sputtered DLC coating, measured at a speed of 0.06 m/s for a load of 10 g. The environment was alternated between oxygen and nitrogen gases [108]

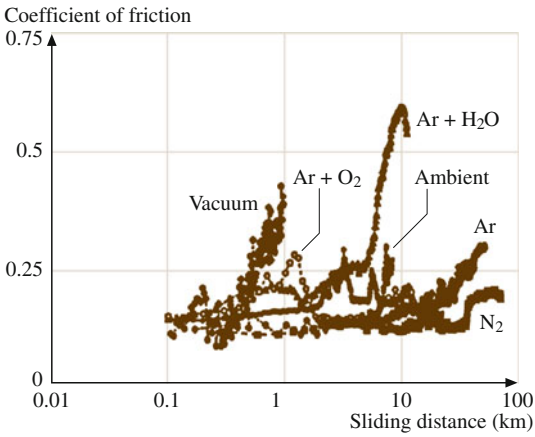

Fig. 17.30 Durability, measured by sliding a Al_2O_3-TiC magnetic slider against a magnetic disk coated with a 20 nm thick DC sputtered amorphous carbon coating and 2 nm thick perfluoropolyether film, measured at a speed of 0.75 m/s and for a load of 10 g. Vacuum refers to 2×10^{-7} Torr [71]

vacuum is even worse. Indeed, failure mechanisms differ in different environments. In high vacuum, intimate contact between the disk and the slider surface results in significant wear. In ambient air, Ar + O_2 and Ar + H_2O, tribochemical oxidation of the carbon overcoat is responsible for interface failure. For experiments performed in pure argon and nitrogen, mechanical shearing of the asperities causes the formation of debris, which is responsible for the formation of scratch marks on the carbon surface, which were observed with an optical microscope [71].

Functional Tests

Magnetic thin film heads made with Al_2O_3–TiC substrate are used in magnetic storage applications [13]. A multilayered thin film pole–tip structure present on the head surface wears more rapidly than the much harder Al_2O_3–TiC substrate. Pole–tip recession (PTR) is a serious concern in magnetic storage [15–19, 112]. Two of the diamond-like carbon coatings with superior mechanical properties – ion beam and cathodic arc carbon coatings – were deposited on the air-bearing surfaces of

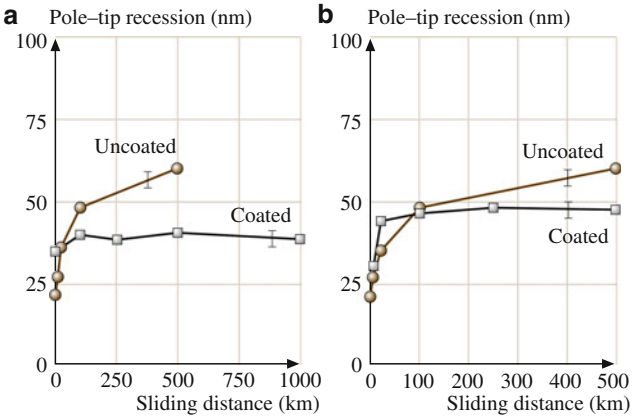

Fig. 17.31 Pole–tip recession as a function of sliding distance, measured with an AFM, for **(a)** uncoated and 20 nm thick ion beam carbon coated, and **(b)** uncoated and 20 nm thick cathodic arc carbon coated Al_2O_3–TiC heads run against MP tapes [15]

Al_2O_3–TiC head sliders [15]. Functional tests were conducted by running a metal particle (MP) tape in a computer tape drive. The average PTR as a function of sliding distance is presented in Fig. 17.31. We note that the PTR increases for the uncoated head, whereas there is a slight increase in PTR for the coated heads during early sliding followed by little change. Thus, the coatings provide protection.

The micromechanical as well as the accelerated and functional tribological data presented here clearly suggest that there is a good correlation between the scratch resistance and wear resistance measured using accelerated tests and functional tests. Thus, scratch tests can be successfully used to screen coatings for wear applications.

17.3.4 Coating Continuity Analysis

Ultrathin (less than 10 nm) coatings may not uniformly coat the sample surface. In other words, the coating may be discontinuous and deposited in the form of islands on the microscale. Therefore, one possible reason for poor wear protection and the nonuniform failure of thin coatings may be poor coverage of the substrate. Coating continuity can be studied using surface analytical techniques such as Auger and/or XPS analyses. Any discontinuity in coating thickness that is less than the sampling depth of the instrument result in the local detection of the substrate species [49, 50, 102].

The results from an XPS analysis of 1.3 mm^2 regions (single point measurement with spot diameter of 1,300 μm) on various coatings deposited on Si(100) substrates are shown in Fig. 17.32. The sampling depth is about 2–3 nm. The poor SP coatings and the poor 5 nm and 3.5 nm FCA coatings () show much lower carbon

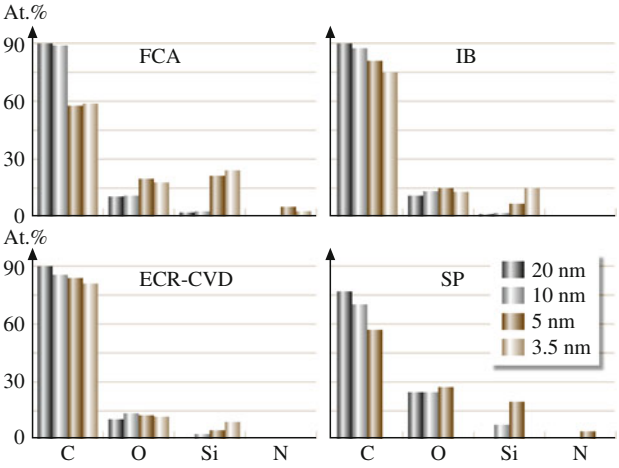

Fig. 17.32 Quantified XPS data for various DLC coatings on Si(100) substrate [50]. Atomic concentrations are shown

contents (atomic concentrations of <75% and <60% respectively) than the IB and ECR-CVD coatings. Silicon is detected in all of the 5 nm coatings. From the data it is hard to infer whether the Si is from the substrate or from exposed regions due to discontinuous coating. Based on the sampling depth, any Si detected in 3.5 nm coatings would likely be from the substrate. The other interesting observation is that all poor coatings (all SP and FCA 5 and 3.5 nm coatings) have almost twice the oxygen content of the other coatings. Any oxygen present may be due to leaks in the deposition chamber, and it is present as silicon oxides.

AES measurements averaged over a scan area of 900 μm^2 were conducted on FCA and SP 5 nm coatings at six different regions on each sample. Very little silicon was detected on this scale, and the detected peaks were characteristic of oxides. The oxygen levels were comparable to those seen for good coatings via XPS. These results contrast with the XPS measurements performed at a larger scale, suggesting that the coatings only possess discontinuities at isolated areas and that the 5 nm coatings are generally continuous on the microscale. Figure 17.33 shows representative XPS and AES spectra of selected samples.

17.4 Closure

Diamond material and its smooth coatings are used for very low wear and relatively low friction. Major limitations of the true diamond coatings are that they need to be deposited at high temperatures, can only be deposited on selected substrates, and require surface finishing. Hard amorphous carbon (a-C) or commonly known as DLC coatings exhibit mechanical, thermal and optical properties close to that of

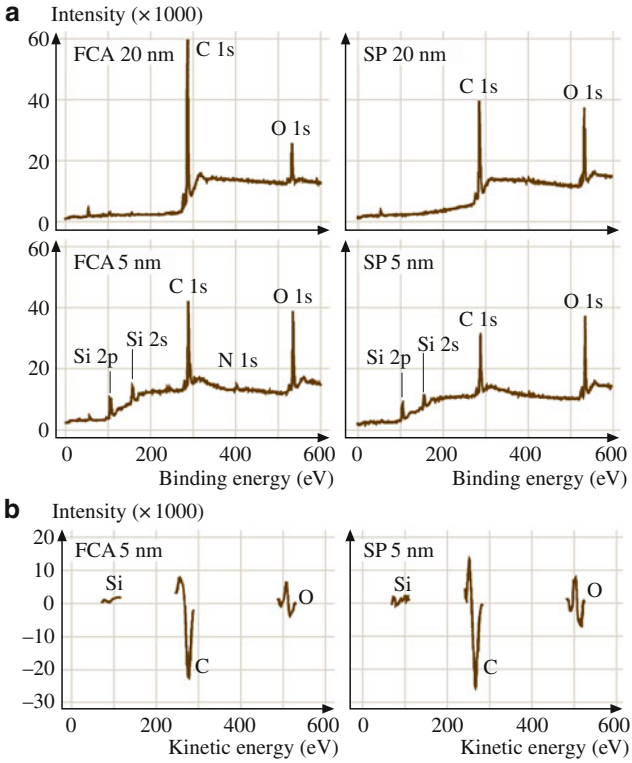

Fig. 17.33 **(a)** XPS spectra for 5 nm and 20 nm thick FCA and SP coatings on Si(100) substrate, and **(b)** AES spectra for FCA and SP coatings of 5 nm thickness on Si(100) substrate [50]

diamond. These can be deposited with a large range of thicknesses by using a variety of deposition processes, on variety of substrates at or near room temperature. The coatings reproduce substrate topography avoiding the need of post finishing. Friction and wear properties of some DLC coatings can be very attractive for tribological applications. The largest industrial application of these coatings is in magnetic storage devices. They are expected to be used in MEMS/NEMS.

EELS and Raman spectroscopies can be successfully used for chemical characterization of amorphous carbon coatings. The prevailing atomic arrangement in the DLC coatings is amorphous or quasi-amorphous with small diamond (sp^3), graphite (sp^2) and other unidentifiable micro- or nanocrystallites. Most DLC coatings except those produced by filtered cathodic arc contain from a few to about 50 at.% hydrogen. Sometimes hydrogen is deliberately incorporated in the sputtered and ion plated coatings to tailor their properties.

Amorphous carbon coatings deposited by various techniques exhibit different mechanical and tribological properties. The nanoindenter can be successfully used for measurement of hardness, elastic modulus, fracture toughness, and fatigue life. Microscratch and microwear experiments can be performed using either

a nanoindenter or an AFM. Thin coatings deposited by filtered cathodic arc, ion beam and ECR-CVD hold a promise for tribological applications. Coatings as thin as 5 nm or even thinner in thickness provide wear protection. Microscratch, microwear, and accelerated wear testing, if simulated properly can be successfully used to screen coating candidates for industrial applications. In the examples shown in this chapter, trends observed in the microscratch, microwear, and accelerated macrofriction wear tests are similar to that found in functional tests.

References

1. B. Bhushan, B.K. Gupta, *Handbook of Tribology: Materials, Coatings, and Surface Treatments* (Krieger, Malabar, 1997)
2. B. Bhushan, *Principles and Applications of Tribology* (Wiley, New York, 1999)
3. B. Bhushan, *Introduction to Tribology* (Wiley, New York, 2002)
4. B. Bhushan, B.K. Gupta, G.W. VanCleef, C. Capp, J.V. Coe: Fullerene (C_60) films for solid lubrication. Tribol. Trans. **36**, 573–580 (1993)
5. B.K. Gupta, B. Bhushan, C. Capp, J.V. Coe, Material characterization and effect of purity and ion implantation on the friction and wear of sublimed fullerene films. J. Mater. Res. **9**, 2823–2838 (1994)
6. B.K. Gupta, B. Bhushan, Fullerene particles as an additive to liquid lubricants and greases for low friction and wear. Lubr. Eng. **50**, 524–528 (1994)
7. B. Bhushan, V.V. Subramaniam, A. Malshe, B.K. Gupta, J. Ruan, Tribological properties of polished diamond films. J. Appl. Phys. **74**, 4174–4180 (1993)
8. B. Bhushan, B.K. Gupta, V.V. Subramaniam, Polishing of diamond films, Diam. Films Technol. **4**, 71–97 (1994)
9. P. Sander, U. Kaiser, M. Altebockwinkel, L. Wiedmann, A. Benninghoven, R.E. Sah, P. Koidl, Depth profile analysis of hydrogenated carbon layers on silicon by x-ray photoelectron spectroscopy, auger electron spectroscopy, electron energy-loss spectroscopy, and secondary ion mass spectrometry. J. Vac. Sci. Technol. A **5**, 1470–1473 (1987)
10. A. Matthews, S.S. Eskildsen, Engineering applications for diamond-like carbon. Diam. Relat. Mater. **3**, 902–911 (1994)
11. A.H. Lettington, Applications of diamond-like carbon thin films. Carbon **36**, 555–560 (1998)
12. B.K. Gupta, B. Bhushan, Mechanical and tribological properties of hard carbon coatings for magnetic recording heads. Wear **190**, 110–122 (1995)
13. B. Bhushan, *Tribology and Mechanics of Magnetic Storage Devices*, 2nd edn. (Springer, Heidelberg, 1996)
14. B. Bhushan, *Mechanics and Reliability of Flexible Magnetic Media*, 2nd edn. (Springer, Heidelberg, 2000)
15. B. Bhushan, S.T. Patton, R. Sundaram, S. Dey, Pole tip recession studies of hard carbon-coated thin-film tape heads. J. Appl. Phys. **79**, 5916–5918 (1996)
16. J. Xu, B. Bhushan, Pole tip recession studies of thin-film rigid disk head sliders II: Effects of air bearing surface and pole tip region designs and carbon coating. Wear **219**, 30–41 (1998)
17. W.W. Scott, B. Bhushan, Corrosion and wear studies of uncoated and ultra-thin DLC coated magnetic tape-write heads and magnetic tapes. Wear **243**, 31–42 (2000)
18. W.W. Scott, B. Bhushan, Loose debris and head stain generation and pole tip recession in modern tape drives. J. Inf. Storage Proc. Syst. **2**, 221–254 (2000)
19. W.W. Scott, B. Bhushan, A.V. Lakshmikumaran, Ultrathin diamond-like carbon coatings used for reduction of pole tip recession in magnetic tape heads. J. Appl. Phys. **87**, 6182–6184 (2000)

20. B. Bhushan, Macro- and microtribology of magnetic storage devices. In *Modern Tribology Handbook*, ed. by B. Bhushan (CRC, Boca Raton, 2001) pp.1413–1513
21. B. Bhushan, Nanotribology and nanomechanics of MEMS devices. *Proc. 9th Annu. Workshop Micro Electro Mech. Syst.* (IEEE, New York, 1996) pp.91–98
22. B. Bhushan (Ed.), *Tribology Issues and Opportunities in MEMS* (Kluwer, Dordrecht, 1998)
23. B. Bhushan: *Handbook of Micro/Nanotribology*, 2nd edn. (CRC, Boca Raton 1999)
24. B. Bhushan, Macro- and microtribology of MEMS materials. In *Modern Tribology Handbook*, ed. by B. Bhushan (CRC, Boca Raton, 2001) pp.1515–1548
25. S. Aisenberg, R. Chabot, Ion beam deposition of thin films of diamond-like carbon. J. Appl. Phys. **49**, 2953–2958 (1971)
26. E.G. Spencer, P.H. Schmidt, D.C. Joy, F.J. Sansalone, Ion beam deposited polycrystalline diamond-like films. Appl. Phys. Lett. **29**, 118–120 (1976)
27. A. Grill, B.S. Meyerson, Development and status of diamondlike carbon. In *Synthetic Diamond: Emerging CVD Science and Technology*, ed. by K.E. Spear, J.P. Dismukes (Wiley, New York, 1994) pp.91–141
28. Y. Catherine, Preparation techniques for diamond-like carbon. In *Diamond and Diamond-Like Films and Coatings*, ed. by R.E. Clausing, L.L. Horton, J.C. Angus, P. Koidl (Plenum, New York, 1991), pp.193–227
29. J.J. Cuomo, D.L. Pappas, J. Bruley, J.P. Doyle, K.L. Seagner, Vapor deposition processes for amorphous carbon films with sp^3 fractions approaching diamond. J. Appl. Phys. **70**, 1706–1711 (1991)
30. J.C. Angus, C.C. Hayman, Low pressure metastable growth of diamond and diamondlike phase. Science **241**, 913–921 (1988)
31. J.C. Angus, F. Jensen, Dense diamondlike hydrocarbons as random covalent networks. J. Vac. Sci. Technol. A **6**, 1778–1782 (1988)
32. D.C. Green, D.R. McKenzie, P.B. Lukins, The microstructure of carbon thin films. Mater. Sci. Forum **52/53**, 103–124 (1989)
33. N.H. Cho, K.M. Krishnan, D.K. Veirs, M.D. Rubin, C.B. Hopper, B. Bhushan, D.B. Bogy, Chemical structure and physical properties of diamond-like amorphous carbon films prepared by magnetron sputtering. J. Mater. Res. **5**, 2543–2554 (1990)
34. J.C. Angus, Diamond and diamondlike films, Thin Solid Films **216**, 126–133 (1992)
35. B. Bhushan, A.J. Kellock, N.H. Cho, J.W. Ager III, Characterization of chemical bonding and physical characteristics of diamond-like amorphous carbon and diamond films. J. Mater. Res. **7**, 404–410 (1992)
36. J. Robertson, Properties of diamond-like carbon. Surf. Coat. Technol. **50**, 185–203 (1992)
37. N. Savvides, B. Window, Diamondlike amorphous carbon films prepared by magnetron sputtering of graphite, J. Vac. Sci. Technol. A **3**, 2386–2390 (1985)
38. J.C. Angus, P. Koidl, S. Domitz, Carbon thin films. In, *Plasma Deposited Thin Films*, ed. by J. Mort, F. Jensen (CRC, Boca Raton, 1986) pp.89–127
39. J. Robertson, Amorphous carbon, Adv. Phys. **35**, 317–374 (1986)
40. M. Rubin, C.B. Hooper, N.H. Cho, B. Bhushan, Optical and mechanical properties of DC sputtered carbon films. J. Mater. Res. **5**, 2538–2542 (1990)
41. G.J. Vandentop, M. Kawasaki, R.M. Nix, I.G. Brown, M. Salmeron, G.A. Somorjai, Formation of hydrogenated amorphous carbon films of controlled hardness from a methane plasma. Phys. Rev. B **41**, 3200–3210 (1990)
42. J.J. Cuomo, D.L. Pappas, R. Lossy, J.P. Doyle, J. Bruley, G.W. Di Bello, W. Krakow, Energetic carbon deposition at oblique angles. J. Vac. Sci. Technol. A **10**, 3414–3418 (1992)
43. D.L. Pappas, K.L. Saenger, J. Bruley, W. Krakow, J.J. Cuomo, Pulsed laser deposition of diamondlike carbon films. J. Appl. Phys. **71**, 5675–5684 (1992)
44. H.J. Scheibe, B. Schultrich, DLC film deposition by laser-arc and study of properties. Thin Solid Films **246**, 92–102 (1994)
45. C. Donnet, A. Grill, Friction control of diamond-like carbon coatings. Surf. Coat. Technol. **94/95**, 456 (1997)

46. A. Grill, Tribological properties of diamondlike carbon and related materials. Surf. Coat. Technol. **94/95**, 507 (1997)
47. B.K. Gupta, B. Bhushan, Micromechanical properties of amorphous carbon coatings deposited by different deposition techniques. Thin Solid Films **270**, 391–398 (1995)
48. X. Li, B. Bhushan, Micro/nanomechanical and tribological characterization of ultra-thin amorphous carbon coatings. J. Mater. Res. **14**, 2328–2337 (1999)
49. X. Li, B. Bhushan, Mechanical and tribological studies of ultra-thin hard carbon overcoats for magnetic recording heads. Z. Metallkd. **90**, 820–830 (1999)
50. S. Sundararajan, B. Bhushan, Micro/nanotribology of ultra-thin hard amorphous carbon coatings using atomic force/friction force microscopy. Wear **225–229**, 678–689 (1999)
51. B. Bhushan, Chemical, mechanical, and tribological characterization of ultra-thin and hard amorphous carbon coatings as thin as 3.5 nm: Recent developments. Diam. Relat. Mater. **8**, 1985–2015 (1999)
52. I.I. Aksenov, V.E. Strel'Nitskii, Wear resistance of diamond-like carbon coatings. Surf. Coat. Technol. **47**, 252–256 (1991)
53. D.R. McKenzie, D. Muller, B.A. Pailthorpe, Z.H. Wang, E. Kravtchinskaia, D. Segal, P.B. Lukins, P.J. Martin, G. Amaratunga, P.H. Gaskell, A. Saeed, Properties of tetrahedral amorphous carbon prepared by vacuum arc deposition. Diam. Relat. Mater. **1**, 51–59 (1991)
54. R. Lossy, D.L. Pappas, R.A. Roy, J.J. Cuomo, Filtered arc deposition of amorphous diamond. Appl. Phys. Lett. **61**, 171–173 (1992)
55. I.G. Brown, A. Anders, S. Anders, M.R. Dickinson, I.C. Ivanov, R.A. MacGill, X.Y. Yao, K.M. Yu, Plasma synthesis of metallic and composite thin films with atomically mixed substrate bonding. Nucl. Instrum. Methods. B **80/81**, 1281–1287 (1993)
56. P.J. Fallon, V.S. Veerasamy, C.A. Davis, J. Robertson, G.A.J. Amaratunga, W.I. Milne, J. Koskinen, Properties of filtered-ion-beam-deposited diamond-like carbon as a function of ion energy. Phys. Rev. B **48**, 4777–4782 (1993)
57. S. Anders, A. Anders, I.G. Brown, B. Wei, K. Komvopoulos, J.W. Ager III, K.M. Yu: Effect of vacuum arc deposition parameters on the properties of amorphous carbon thin films, Surf. Coat. Technol. **68/69**, 388–393 (1994)
58. S. Anders, A. Anders, I.G. Brown, M.R. Dickinson, R.A. MacGill, Metal plasma immersion ion implantation and deposition using arc plasma sources. J. Vac. Sci. Technol. B **12**, 815–820 (1994)
59. S. Anders, A. Anders, I.G. Brown, Transport of vacuum arc plasma through magnetic macroparticle filters. Plasma Sources Sci. **4**, 1–12 (1995)
60. D.M. Swec, M.J. Mirtich, B.A. Banks, *Ion Beam and Plasma Methods of Producing Diamondlike Carbon Films* (NASA, Cleveland, 1989). Report No. NASA TM102301
61. A. Erdemir, M. Switala, R. Wei, P. Wilbur, A tribological investigation of the graphite-to-diamond-like behavior of amorphous carbon films ion beam deposited on ceramic substrates. Surf. Coat. Technol. **50**, 17–23 (1991)
62. A. Erdemir, F.A. Nicols, X.Z. Pan, R. Wei, P.J. Wilbur, Friction and wear performance of ion-beam deposited diamond-like carbon films on steel substrates. Diam. Relat. Mater. **3**, 119–125 (1993)
63. R. Wei, P.J. Wilbur, M.J. Liston, Effects of diamond-like hydrocarbon films on rolling contact fatigue of bearing steels. Diam. Relat. Mater. **2**, 898–903 (1993)
64. A. Erdemir, C. Donnet, Tribology of diamond, diamond-like carbon, and related films. In *Modern Tribology Handbook*, ed. by B. Bhushan (CRC, Boca Raton, 2001), pp. 871–908
65. J. Asmussen, Electron cyclotron resonance microwave discharges for etching and thin-film deposition. J. Vac. Sci. Technol. A **7**, 883–893 (1989)
66. J. Suzuki, S. Okada, Deposition of diamondlike carbon films using electron cyclotron resonance plasma chemical vapor deposition from ethylene gas. Jpn. J. Appl. Phys. **34**, L1218–L1220 (1995)
67. B.A. Banks, S.K. Rutledge, Ion beam sputter deposited diamond like films. J. Vac. Sci. Technol. **21**, 807–814 (1982)

68. C. Weissmantel, K. Bewilogua, K. Breuer, D. Dietrich, U. Ebersbach, H.J. Erler, B. Rau, G. Reisse, Preparation and properties of hard i-C and i-BN coatings. Thin Solid Films **96**, 31–44 (1982)
69. H. Dimigen, H. Hubsch, Applying low-friction wear-resistant thin solid films by physical vapor deposition. Philips Tech. Rev. **41**, 186–197 (1983)
70. B. Bhushan, B.K. Gupta, M.H. Azarian, Nanoindentation, microscratch, friction and wear studies for contact recording applications. Wear **181–183**, 743–758 (1995)
71. B. Bhushan, L. Yang, C. Gao, S. Suri, R.A. Miller, B. Marchon, Friction and wear studies of magnetic thin-film rigid disks with glass-ceramic, glass and aluminum-magnesium substrates. Wear **190**, 44–59 (1995)
72. L. Holland, S.M. Ojha, Deposition of hard and insulating carbonaceous films of an RF target in butane plasma. Thin Solid Films **38**, L17–L19 (1976)
73. L.P. Andersson, A review of recent work on hard i-C films. Thin Solid Films **86**, 193–200 (1981)
74. A. Bubenzer, B. Dischler, B. Brandt, P. Koidl, RF plasma deposited amorphous hydrogenated hard carbon thin films, preparation, properties and applications. J. Appl. Phys. **54**, 4590–4594 (1983)
75. A. Grill, B.S. Meyerson, V.V. Patel, Diamond-like carbon films by RF plasma-assisted chemical vapor deposition from acetylene. IBM J. Res. Dev. **34**, 849–857 (1990)
76. A. Grill, B.S. Meyerson, V.V. Patel, Interface modification for improving the adhesion of a-C:H to metals. J. Mater. Res. **3**, 214 (1988)
77. A. Grill, V.V. Patel, B.S. Meyerson, Optical and tribological properties of heat-treated diamond-like carbon. J. Mater. Res. **5**, 2531–2537 (1990)
78. F. Jansen, M. Machonkin, S. Kaplan, S. Hark, The effect of hydrogenation on the properties of ion beam sputter deposited amorphous carbon. J. Vac. Sci. Technol. A **3**, 605–609 (1985)
79. S. Kaplan, F. Jansen, M. Machonkin, Characterization of amorphous carbon-hydrogen films by solid-state nuclear magnetic resonance. Appl. Phys. Lett. **47**, 750–753 (1985)
80. H.C. Tsai, D.B. Bogy, M.K. Kundmann, D.K. Veirs, M.R. Hilton, S.T. Mayer, Structure and properties of sputtered carbon overcoats on rigid magnetic media disks. J. Vac. Sci. Technol. A **6**, 2307–2315 (1988)
81. B. Marchon, M. Salmeron, W. Siekhaus, Observation of graphitic and amorphous structures on the surface of hard carbon films by scanning tunneling microscopy. Phys. Rev. B **39**, 12907–12910 (1989)
82. B. Dischler, A. Bubenzer, P. Koidl, Hard carbon coatings with low optical absorption. Appl. Phys. Lett. **42**, 636–638 (1983)
83. D.S. Knight, W.B. White, Characterization of diamond films by Raman spectroscopy. J. Mater. Res. **4**, 385–393 (1989)
84. J.W. Ager III, D.K. Veirs, C.M. Rosenblatt, Spatially resolved Raman studies of diamond films grown by chemical vapor deposition. Phys. Rev. B **43**, 6491–6499 (1991)
85. W. Scharff, K. Hammer, O. Stenzel, J. Ullman, M. Vogel, T. Frauenheim, B. Eibisch, S. Roth, S. Schulze, I. Muhling, Preparation of amorphous i-C films by ion-assisted methods. Thin Solid Films **171**, 157–169 (1989)
86. B. Bhushan, X. Li, Nanomechanical characterization of solid surfaces and thin films. Int. Mater. Rev. **48**, 125–164 (2003)
87. X. Li, D. Diao, B. Bhushan, Fracture mechanisms of thin amorphous carbon films in nanoindentation. Acta Mater. **45**, 4453–4461 (1997)
88. X. Li, B. Bhushan, Measurement of fracture toughness of ultra-thin amorphous carbon films. Thin Solid Films **315**, 214–221 (1998)
89. X. Li, B. Bhushan, Evaluation of fracture toughness of ultra-thin amorphous carbon coatings deposited by different deposition techniques. Thin Solid Films **355/356**, 330–336 (1999)
90. X. Li, B. Bhushan, Development of a nanoscale fatigue measurement technique and its application to ultrathin amorphous carbon coatings. Scr. Mater. **47**, 473–479 (2002)
91. X. Li, B. Bhushan, Nanofatigue studies of ultrathin hard carbon overcoats used in magnetic storage devices. J. Appl. Phys. **91**, 8334–8336 (2002)

92. J. Robertson, Deposition of diamond-like carbon. Philos. Trans. R. Soc. Lond. A **342**, 277–286 (1993)
93. S.J. Bull, Tribology of carbon coatings: DLC, diamond and beyond. Diam. Relat. Mater. **4**, 827–836 (1995)
94. N. Savvides, T.J. Bell, Microhardness and Young's modulus of diamond and diamondlike carbon films. J. Appl. Phys. **72**, 2791–2796 (1992)
95. B. Bhushan, M.F. Doerner, Role of mechanical properties and surface texture in the real area of contact of magnetic rigid disks. ASME J. Tribol. **111**, 452–458 (1989)
96. S. Suresh, *Fatigue of Materials* (Cambridge University Press, Cambridge, 1991)
97. D.B. Marshall, A.G. Evans, Measurement of adherence of residual stresses in thin films by indentation. I. Mechanics of interface delamination. J. Appl. Phys. **15**, 2632–2638 (1984)
98. A.G. Evans, J.W. Hutchinson, On the mechanics of delamination and spalling in compressed films. Int. J. Solids Struct. **20**, 455–466 (1984)
99. S. Sundararajan, B. Bhushan, Development of a continuous microscratch technique in an atomic force microscope and its application to study scratch resistance of ultrathin hard amorphous carbon coatings. J. Mater. Res. **16**, 437–445 (2001)
100. B. Bhushan, B.K. Gupta, Micromechanical characterization of Ni-P coated aluminum-magnesium, glass and glass-ceramic substrates and finished magnetic thin-film rigid disks. Adv. Inf. Storage Syst. **6**, 193–208 (1995)
101. X. Li, B. Bhushan, Micromechanical and tribological characterization of hard amorphous carbon coatings as thin as 5 nm for magnetic recording heads. Wear **220**, 51–58 (1998)
102. B. Bhushan, V.N. Koinkar, Microscale mechanical and tribological characterization of hard amorphous coatings as thin as 5 nm for magnetic disks. Surf. Coat. Technol. **76/77**, 655–669 (1995)
103. V.N. Koinkar, B. Bhushan, Microtribological properties of hard amorphous carbon protective coatings for thin-film magnetic disks and heads. Proc. Inst. Mech. Eng. J **211**, 365–372 (1997)
104. T.W. Wu, Microscratch and load relaxation tests for ultra-thin films. J. Mater. Res. **6**, 407–426 (1991)
105. R. Memming, H.J. Tolle, P.E. Wierenga, Properties of polymeric layers of hydrogenated amorphous carbon produced by plasma-activated chemical vapor deposition: tribological and mechanical properties. Thin Solid Films **143**, 31–41 (1986)
106. C. Donnet, T. Le Mogne, L. Ponsonnet, M. Belin, A. Grill, V. Patel, The respective role of oxygen and water vapor on the tribology of hydrogenated diamond-like carbon coatings. Tribol. Lett. **4**, 259 (1998)
107. F.P. Bowden, J.E. Young, Friction of diamond, graphite and carbon and the influence of surface films. Proc. R. Soc. Lond. A **208**, 444–455 (1951)
108. B. Marchon, N. Heiman, M.R. Khan, Evidence for tribochemical wear on amorphous carbon thin films. IEEE Trans. Magn. **26**, 168–170 (1990)
109. M.T. Dugger, Y.W. Chung, B. Bhushan, W. Rothschild, Friction, wear, and interfacial chemistry in thin film magnetic rigid disk files. ASME J. Tribol. **112**, 238–245 (1990)
110. B.D. Strom, D.B. Bogy, C.S. Bhatia, B. Bhushan, Tribochemical effects of various gases and water vapor on thin film magnetic disks with carbon overcoats. ASME J. Tribol. **113**, 689–693 (1991)
111. B. Bhushan, J. Ruan, Tribological performance of thin film amorphous carbon overcoats for magnetic recording rigid disks in various environments. Surf. Coat. Technol. **68/69**, 644–650 (1994)
112. B. Bhushan, G.S.A.M. Theunissen, X. Li, Tribological studies of chromium oxide films for magnetic recording applications. Thin Solid Films **311**, 67–80 (1997)